BRD4 represses developmental and neuronal genes through interactions with polycomb complexes

Fanny Boulet[1, 2*], Manthan Patel[1, 2*], Zeinab S. Zanjani[1, 2], Nuria Andres-Sanchez[1, 2], Anam Ijaz[1, 2], Debosree Pal[1], Pankaj Dubey[1], Aoife Murray[1], Dean Nizetic[1], Michael D. LeClaire[3], Karina L. Bursch[3], Brian C. Smith[3] and Madapura M Pradeepa[1, 2#]

1 Blizard Institute, Centre for Genomics and Child Health, Barts and The London School of Medicine and Dentistry, Queen Mary University of London, London, E1 2AT.

2 Centre for Epigenetics, Barts and The London School of Medicine and Dentistry, Queen Mary University of London, London, E1 2AT.

3 Department of Biochemistry, Program in Chemical Biology, Medical College of Wisconsin, Milwaukee, Wisconsin 53226, United States.

* Equal first authors

Correspondence to Madapura M Pradeepa: p.m.madapura@qmul.ac.uk

Highlights

- Acute degradation of BRD4 leads to upregulation of bivalently marked developmental and neuronal genes.
- BRD4 interacts with components of the PRC1.6 complex and EED.
- BRD4 represses PRC1.6-repressed and bivalent genes
- H3K14ac and H3K23ac roles in recruiting BRD4 to bivalent chromatin
- BRD4-BD2 mutations lead to premature upregulation of neuronal genes, altering neuronal cell fate

Keywords: BRD4, dTAG, histone acetylations, Polycomb, PRC1.6, bivalent genes, stem cells, neural organoids, neurodevelopmental disorders.

Abstract

BRD4 is a member of the bromodomain and extraterminal domain containing protein family, primarily known for regulating transcriptional elongation and enhancer activity. Heterozygous loss-of-function mutations in BRD4 cause craniofacial and neurodevelopmental impairments. However, it remains unclear why mutations in this general transcriptional activator lead to specific neurodevelopmental defects.

Using an in vitro human embryonic brain development model, we demonstrate that BRD4 functions as a repressor of Polycomb-regulated developmental and neuronal genes. Acute degradation or loss-of-function mutations in BRD4 in human embryonic stem cells and neuronal lineage deregulate immediate-early genes important for learning and memory formation. We show that BRD4 interacts with components of the noncanonical Polycomb repressive complex PRC1.6 and co-occupies PRC1.6-bound and bivalently marked promoters (H3K27me3 and H3K4me3). We further demonstrate that H3K14ac and H3K23ac recruit BRD4 to bivalent chromatin via its second bromodomain (BD2). These interaction and co-occupancy data suggest BRD4 could contribute to recruitment or maintenance of PRC1.6 and EED at specific sets of genes. As a result, BRD4 represses key developmental and neuronal transcription factors, as well as genes required for learning and memory formation.

Single-cell RNA-seq and single-cell CUT&Tag analyses in unguided neuronal organoids confirm that BRD4 loss-of-function mutations lead to increased expression of Polycomb-regulated developmental transcription factor families, including ZIC, HOX, PAX, SOX, and POU. Additionally, single-cell chromatin accessibility data reveal that BRD4 mutations increase accessibility at transcription factor motifs normally repressed by BRD4. Neuronal organoids with BRD4 mutations lead to altered neuronal cell fate, particularly increased differentiation towards diencephalic and retinal pigment epithelium, including the appearance of eye-like pigmentation.

Together, these findings uncover a critical role for BRD4 in preventing the premature activation of developmental transcription factors, providing new mechanistic insights into the pathogenesis of congenital neurodevelopmental disorders.

Introduction

Acetylated lysine residues are recognized by bromodomain (BD) containing proteins, including bromodomain and extra-terminal domain (BET) proteins– BRD2, BRD3 and BRD4 [1]. BET proteins have two conserved N-terminal bromodomains, which recognize acetylated lysine residues and are enriched at active enhancers and promoters. BET proteins have non-redundant functions in regulating chromatin structure, transcription and DNA repair [2–4]. BRD4 interacts with multiple protein partners to regulate diverse nuclear processes, including transcriptional pause release, elongation, splicing, DNA repair, and maintenance of genomic stability [5]. BRD4 is enriched at active enhancers and promoters, and very high levels of BRD4 occupancy are characteristic of super-enhancers [6–9].

However, emerging evidence suggests that BRD4 contributes to transcriptional repression. The alternatively spliced short isoform (BRD4-S) promotes HIV-1 latency by repressing HIV transcription [10]. The long isoform (BRD4-L), which contains the *C*-terminal domain (CTD), suppresses the transcription of human papillomavirus genes [11]. BRD4 also interacts with multiple proteins involved in chromatin compaction and transcriptional repression, including polycomb repressive complex 2 (PRC2) subunit embryonic ectoderm development (EED) [12] and the H3K9 methyltransferase G9a [13]. The *Drosophila* ortholog of BRD4 also interacts with polycomb repressive complex 1 (PRC1)[14]. Recent studies support a PRC2-independent role for PRC1 in active gene transcription, particularly during nervous system development [12]. These studies underscore the complex interplay between activating and repressor complexes, which fine-tunes gene expression programmes in a context-dependent manner. However, how BRD4 contributes to regulating transcriptional repression by associating with PRC1 or PRC2 is unclear.

The central nervous system (CNS) is particularly susceptible to perturbations of histone acetylation. Mutations in genes involved in histone acetylation pathways lead to diverse neurodevelopmental and neurological disorders [15–18]. BRD4 plays a key role in neuronal activation and transcriptional responses during memory formation [19]. We previously demonstrated that mutations in BRD4 cause a neurodevelopmental disorder (NDD) with an atypical Cornelia de Lange Syndrome (CdLS) phenotype [16]. Mouse embryonic stem cells (mESCs) harbouring a CdLS mutation in the second bromodomain (BD2) of BRD4 exhibit defective DNA damage signalling and repair [20]. However, the mechanism by which BRD4 perturbations cause specific phenotypes in neurodevelopmental disorders remains poorly understood.

Here, we aimed to define the roles of BRD4 in regulating neuronal chromatin and gene expression using human embryonic stem cells (hESCs), neurons, and unguided neural organoids (UNOs). Using acute degradation combined with multimodal single-cell omics approaches, we demonstrate that BRD4 represses bivalently regulated developmental and neuronal genes by interacting with the noncanonical PRC1 complex PRC1.6. Furthermore, loss-of-function mutations in BRD4 upregulate PRC-regulated neuronal genes and influence neuronal cell fate. Taken together, our results define novel roles for BRD4 in the precise regulation of CNS development and function through transcriptional repression.

Results

BRD4 represses neurodevelopmental genes in stem cells.

Genetic knockout, loss-of-function mutations, or prolonged depletion of BRD4 can have pleiotropic consequences. To circumvent the deleterious impacts of long-term BRD4 protein loss, we profiled the effects of short-term BRD4 protein loss in hESCs, hESC-derived neurons, and UNOs using proteolysis-targeting chimera (PROTAC, ZxH-3-26; hereafter, ZxH) [21]. We also generated BRD4-degron-tagged hESCs by knocking in mutant FKBP and an HA tag at the N-terminus of BRD4 [22], followed by degron-tag (dTAG)-mediated acute degradation of BRD4 (Supplementary Fig. 1a)[22]. Together, we investigated the effects of loss-of-function mutations in the BD2 domain of BRD4 in hESCs, hESC-derived neurons, and unguided neural organoids.

Four hours of ZxH treatment in H9 hESCs efficiently depleted both long and short isoforms of BRD4 without affecting BRD3 levels (Fig. 1a). hESCs retained their pluripotency characteristics within four hours of ZxH treatment and 20 hours after drug washout, suggesting that hESCs do not lose pluripotency within 4 hours of BRD4 degradation (Supplementary Fig. 1b). 1-hour dTAGV-1 or dTAG13 treatment in BRD4-dTAG hESCs resulted in near complete degradation of BRD4 (Fig. 1b).

We then performed RNAseq on H9 hESCs treated with ZxH or DMSO for 4, 8, and 20 hours, together with 20 hours of dTAGv1 treatment to BRD4-dTAG hESCs. Independent clustering of fold change values of differentially expressed genes in at least two time points (adj-p-value <0.05) yielded four K-means clusters (C1-C4) (Fig. 1c). C1 is characterized by genes associated with neurodevelopmental functions (Fig. 1c). Genes in C1 were upregulated after 4 and 8 hours of BRD4 degradation and remained upregulated after 20 hours of ZxH and dTAGV-1 treatment in BRD4-dTAG hESCs (Fig. 1c). C2 is defined by genes associated with brain-specific processes, including development and transcription (Fig. 1c). Genes in C2 were upregulated at 8 and 20 hours after ZxH- and dTAGV-1-mediated BRD4 degradation (Fig. 1c). The upregulation of genes in C1 and C2 was attenuated after 20 hours (Fig. 1c), possibly due to degradation of these drugs over time or gross alterations due to long term perturbations. C3 is distinguished by genes associated with cell-cycle processes (Fig. 1c). Genes in C3 were attenuated at 4 and 8 hours of BRD4 degradation, suggesting that acute BRD4 depletion may cause short-term cell-cycle defects. C4 is characterized by genes associated with the DNA damage response, replication, and pluripotency. BRD4 occupancy at most of the differentially expressed genes in H9 hESCs was similar across replicates of BRD4 CUT&Tag data using two independent antibodies (Fig. 1c). BRD4 occupancy at the promoters of C1 and C2 genes (Figs. 1c and 1d), along with early and sustained upregulation of C1 and C2 genes following acute BRD4 degradation, suggests that BRD4 directly represses the transcription of genes related to neuronal and brain-specific development.

BRD4 is enriched at PRC-repressed and bivalent chromatin regions

To define the mechanism by which BRD4 loss upregulates neuronal and developmental genes and to identify the factors associated with BRD4 at these promoters, we performed cleavage under targets & release using nuclease (CUT&RUN) for known BRD4 interactors. These interactors included the cohesin protein RAD21, the cohesin loader NIPBL, the PRC2 protein EED, and the initiating form of RNA Polymerase II (serine 5-phosphorylated, PolII-S5p) in H9 hESCs. As expected, annotation of

peaks using a Hidden Markov Model analysis of chromatin (ChromHMM) states identified enrichment of BRD4 peaks in active enhancer and promoter segments (Fig. 1e). BRD4 peaks were also enriched at PRC-repressed promoters and bivalent promoters characterized by both activating (H3K4me3) and repressive (H3K27me3) histone modifications (Fig. 1e) [23,24]. 1311 peaks overlapped with bivalent promoters and showed enrichment for EED and PolII-S5p. In contrast, 19784 BRD4 peaks were characterized by the binding of PolII-S5p, BRD2, and BRD3, and active histone modifications such as H3K27ac and H3K4me3 (Supplementary Fig. 1c). Although the binding of BRD4 to active regulatory elements is well-characterized, our data demonstrate that BRD4 co-occupies with PRC-marked regions genome-wide in hESCs.

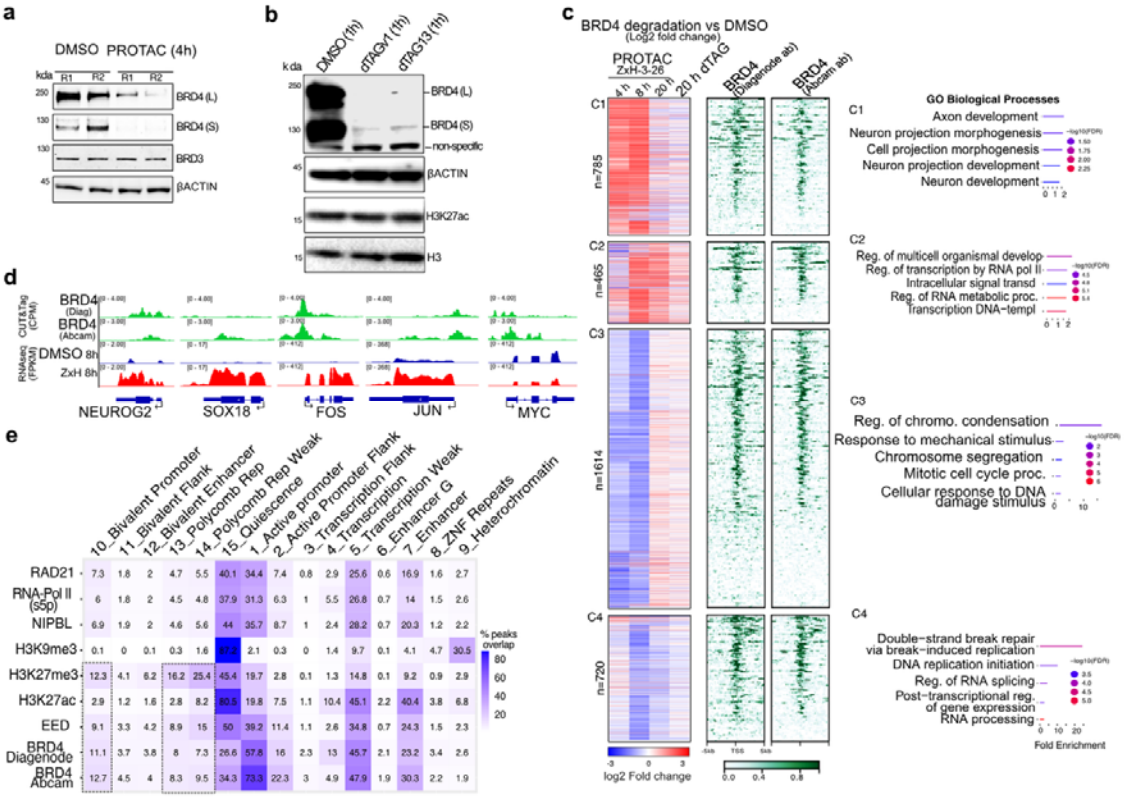

Figure 1: BRD4 degradation upregulates bivalently marked neuronal genes: a and b) Immunoblots showing depletion of BRD4-L and BRD4-S after 4 hours of ZxH-3-26 treatment (ZxH, BRD4-specific PROTAC) (a); dTAGV-1 and dTAG13 mediated BRD4 degradation in BRD4-dTAG hESCs (b), BRD3 and β-ACTIN serve as controls. **c**) Time-course heatmap of RNA-seq data (4 hours, 8 hours, 20 hours) of PROTAC treatment and 20 hours of dTAGV-1 treatment in BRD4-dTAG hESCs comparing log2fold change values across four k-means clusters (C1–C4) based on differential expression levels, indicating similar directional changes at least in two of the ZxH treatment time points (left). Heatmaps of CUT&Tag counts per million reads (CPM) signal for short and long isoforms of BRD4 (Diagenode and Abcam antibodies) (middle). Enrichment of GO biological processes of the genes in the four clusters (right). **d**) Genome-browser visualization of CUT&Tag for BRD4 performed using two antibodies, along with average RNAseq signal (n=3 replicates), performed 8 hours after DMSO and ZxH treatment in H9 hESCs at representative neuronal and developmental genes, along with known BRD4 target gene MYC. **e**) Percentage peak overlap for BRD4, EED, RAD21, NIPBL, serine-5 phosphorylated RNA Pol II (RNA-Pol II s5p), H3K27ac, H3K4me3, and H3K27me3 across 15 ChromHMM states in H9-hESCs.

BRD4 co-occupies and regulates PRC1.6 and bivalent promoters

To further define the mechanism by which BRD4 attenuates expression of neuronal and developmental genes, we analyzed BRD4 CUT&RUN peaks using Cistrome. BRD4 genomic occupancy was similar to that of PRC1.6 component proteins, such as Myc-associated transcriptional regulator X (MAX) and WDR5 (Supplementary Fig 2a). Pairwise peak intersection analysis (Fig. 2a) and signal enrichment at gene promoters showed a higher correlation of BRD4 with PRC1.6, PRC2, and bivalent histone modifications (Fig. 2b). The occupancy of BRD4 with promoters enriched with PRC1.6 and at bivalent marks suggests that BRD4 plays a key role in the regulation of these genes (Fig. 2b).

Based on our observation that BRD4 co-occupies promoters with PRC1.6 and bivalent genes (Figs. 2a and 2b), we determined whether acute BRD4 degradation alters the expression of PRC1.6 target genes. We analyzed public RNA-seq data from PCGF6-knockout (PCGF6-KO) human pluripotent stem cells (hPSCs) to identify genes repressed by BRD4 and PCGF6 [25]. We identified 454 genes that were upregulated in the setting of PCGF6-KO and BRD4 degradation (Fig. 2c); many of these genes are associated with nervous system regulation and brain and heart development. In contrast, 459 downregulated genes are enriched for metabolic processes (Fig. 2c). We classified the promoters of upregulated genes into three groups based on the enrichment of bivalent histone modifications and PRC1.6 and PRC2 proteins (Fig. 2d). Group 1 promoters exhibited high levels of H3K4me3, H3K27ac, BRD4, and PRC1.6 components. These promoters are showed low levels of canonical PRC1 and PRC2 proteins (Fig. 2d). Group 2 promoters were enriched with bivalent histone modifications, PRC2 proteins (EED and EZH2), along with BRD4, and PRC1.6 components (Fig. 2d). Group 3 promoters lacked detectable levels of BRD4 and PRC1.6 components (Fig. 2d). Taken together, our results suggest that BRD4 cooperates with PRC1.6 (PCGF6) and PRC2 components to repress the transcription of developmental and neuronal genes in hESCs.

To assess whether BRD4 directly contributes to the repression of bivalent and PRC1.6 target genes, we performed transient transcriptome sequencing (TT-seq) after 1 hour of dTAG-mediated BRD4 degradation (Fig. 1b). BRD4 degradation led to increased transcription of neuronal genes enriched with bivalent marks at their promoters (LMO2 and OLIG2). Similarly, we observed increased transcription of known PRC1.6 target genes (upregulated following MAX dimerization protein (MGA) knockout in HEK293 cells)[26], such as NEUROG2, YBX2, and SYCE2 (Fig. 2e). These genes are enriched for BRD4 and MAX, which are known to recruit the PRC1.6 complex, and bivalent marks, suggesting that BRD4 represses these genes. MYC transcript levels were reduced, consistent with BRD4's role in regulating MYC transcriptional activation [16]. We observed that nearly 50 % of bivalent genes are upregulated upon 8 hours of ZxH treatment (Supplementary Fig. 2c). Notably, 40% of bivalent genes are upregulated within 4 hours of ZxH treatment, and most of them remain upregulated after 8 and 20 hours. Overall, our findings suggest that BRD4 and PRC1.6 cooperate to repress the transcription of developmental and neuronal genes in hESCs.

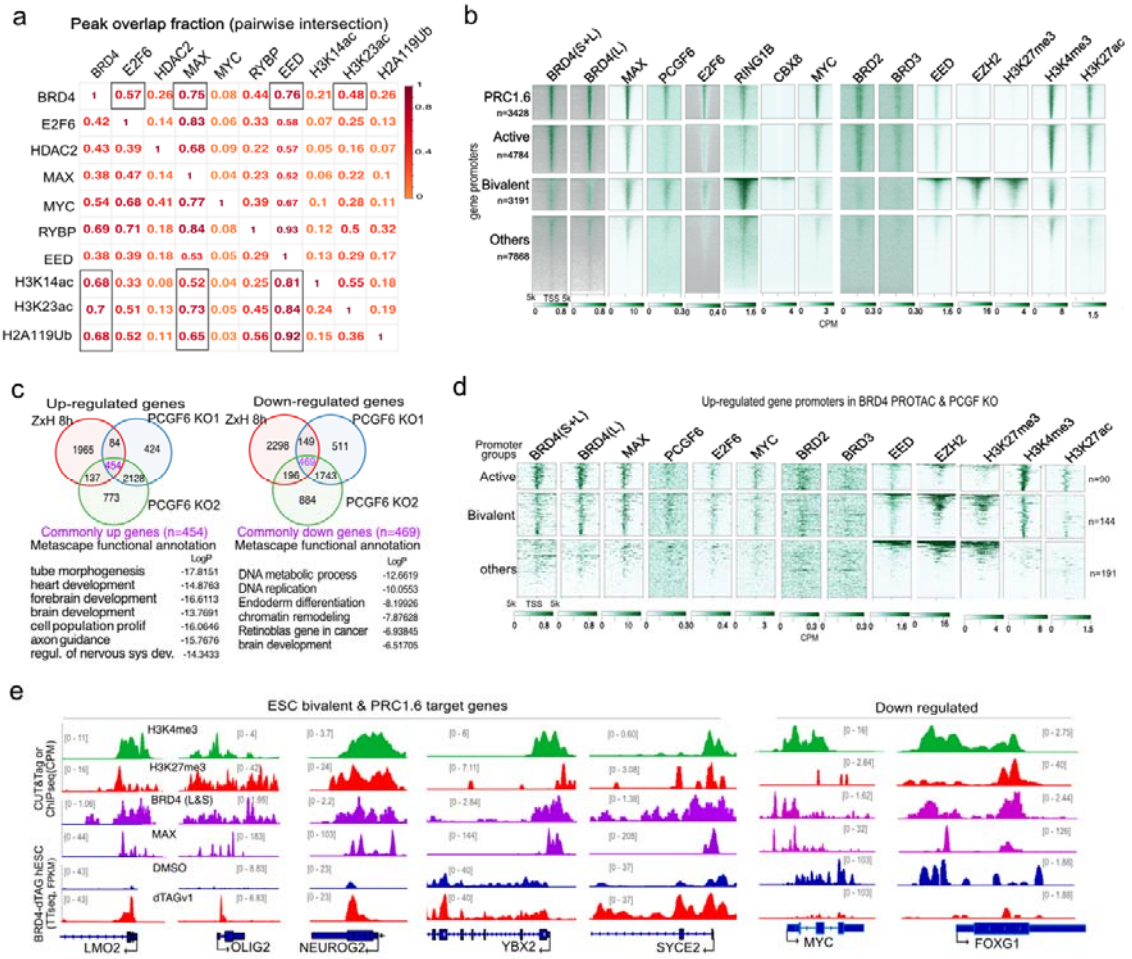

Figure 2: BRD4 occupies and represses PRC target genes. a) Pairwise peak intersection for chromatin modifications. Values indicate the fraction of overlap between peak-sets. Horizontal comparison shows the percentage of overlap between each peak set on the X-axis, with peak sets compared on the Y-axis, and vice versa. **b**) Heatmaps of CUT&Tag counts per million reads (CPM) signal for BRD4 (BRD4, Diagenode antibody), BRD4(Abcam antibody), H3K27me3, H3K4me3, H3K27ac, CUT&RUN for BRD2, BRD3, EED and EZH2, ChIPseq data for PRC1.6 components (PCGF6, MAX, MYC), along with PRC1 component (CBX8 and RING1B). Clustered based on enrichment of PRC1.6 components, active (H3K4me3), bivalent (H3K27me3+ & H3K4me3+), and other gene promoters. **c**) Venn diagrams and Metascape functional annotations (below) of upregulated (left, in purple) and downregulated (right, in purple) genes following 8 hours of ZxH-mediated BRD4 degradation and in two PCGF6 knockout human pluripotent stem cell lines (data from Lan et.al. 2022). **d**) Similar to (b), but clustering based on commonly upregulated genes (clusters 1-3). Upregulated gene promoters are categorized by their bivalent or active chromatin modifications. **e**) Genome-browser visualization of BRD4, MAX, and bivalent histone modifications, along with average TTseq signal (n=3 replicates), performed 1 hour after DMSO and dTAGV-1 treatment in BRD4-dTAG hESCs (Western blotting showing BRD4 degradation in Fig. 1b).

BRD4 interacts with PRC1.6 and PRC2 proteins

To investigate whether BRD4 is specifically associated with PRC complexes, we first analyzed the recently published proximal interactomes of PRC1 (CBX7, RING1B/RNF2, PCGF6) and PRC2

(SUZ12 and EZH2) proteins in mouse ES cells [27]. This analysis identified that BRD4 is enriched in the PRC1.6 complex, as it is enriched in the PCGF6 and RING1B interactome. In contrast, other BET proteins showed low enrichment or were absent (Fig. 3a and Supplementary Fig. 3a). Analysis of publicly available BRD4 IP-mass spectrometry (IP-MS) by Arnold et al 2021 in K562 cells with endogenous HA-dTAG-BRD4 revealed enrichment of PRC1.6 complex subunits (RING1B/RNF2, MGA, PCGF6, CBX3 and WDR5) (Fig. 3b) [28]. IP-MS with an antibody that recognizes only BRD4-L detected PRC1.6 components MGA and CBX3 [29] (Fig. 3b). Similarly, analysis of our published BRD4 IP-MS in mouse ESCs also showed enrichment for PRC1.6 and PRC2 components (Supplementary Fig. 3b) [16]. Notably, no other canonical PRC1 (cPRC1) or noncanonical variant PRC1 (PRC1.1-PRC1.5) complex subunits were detected in these BRD4 interactomes. We validated the interaction between BRD4 and PRC proteins by performing endogenous BRD4 IP using antibodies that recognize both long and short isoforms. Immunoblotting of BRD4 IP detected PRC1.6 proteins RING1B and PCGF6, but not the canonical PRC1 component CBX7 (Fig. 3c). Consistently, reverse IPs with RING1B and MGA antibodies pulled down BRD4 (Fig. 3c). Furthermore, co-immunoprecipitation in HEK293T cells shows interaction of tested PRC1.6 components (E2F6, L3MBTL2), PRC2 protein EED, but not EZH2, with GFP-tagged long isoform of BRD4 (Fig. 3d). Overall, these findings suggest that protein-protein interactions between BRD4 and PRC1.6 and EED could influence their genomic co-occupancy.

BRD4 is recruited to PRC-marked regions through H3K14ac and H3K23ac

PRC2-mediated H3K27me3 antagonizes H3K27ac, so H3K27ac is largely absent at polycomb-repressed and bivalent chromatin. However, nucleosomes with bivalent modifications recruit lysine acetyltransferase 6B (KAT6B), which acetylates H3K14 and H3K23 [30]. We found enrichment of KAT6B in BRD4 IP-MS (Supplementary Fig. 3b) and further validated the interaction of BRD4 with H3K14ac and H3K23ac by performing BRD4 IP immunoblots (Fig. 3c). We found bivalent promoters were enriched for H3K14ac and H3K23ac in hESCs (Fig. 3e), suggesting that these acetyl modifications could be recruiting BRD4 to PRC-repressed bivalent genes. Therefore, we investigated whether the bromodomains of BRD4 contribute to recruiting BRD4 to polycomb chromatin through interaction with H3K14ac and H3K23ac.

We investigated the affinity of BRD4 bromodomains for the H3K14/H3K23 diacetylated H3K14/H3K23ac peptide *in vitro* using AlphaScreen assays (Alpha = amplified luminescent proximity homogeneous assay) (Supplementary Fig. 4a-c). BRD4-BD2, but not BRD4-BD1, robustly bound the H3K14/K23ac peptide (Fig. 3f), consistent with the increased binding of BRD4-BD2 compared to BRD4-BD1 to diacetylated H3 tails [31]. Histone tail peptide pulldown further confirmed that the *N*-terminus of BRD4 containing BD1 and BD2 (amino acids E49-E460) interact with H3K14ac/K23ac; this interaction is sensitive to inhibition by iBET-BD2 (Fig. 3g). Proximity ligation assays (PLA) further confirmed the association of BRD4 with bivalent chromatin regions (Supplementary Fig. 4d). Furthermore, the number of BRD4-H3K23ac and BRD4-H3K27me3 PLA foci decreased after hESCs were treated with an inhibitor against the second bromodomain of all BET proteins (iBET-BD2) (Supplementary Fig. 4d)[32]. Therefore, the BRD4 bromodomains may be required for the association of the full-length protein with bivalent chromatin regions.

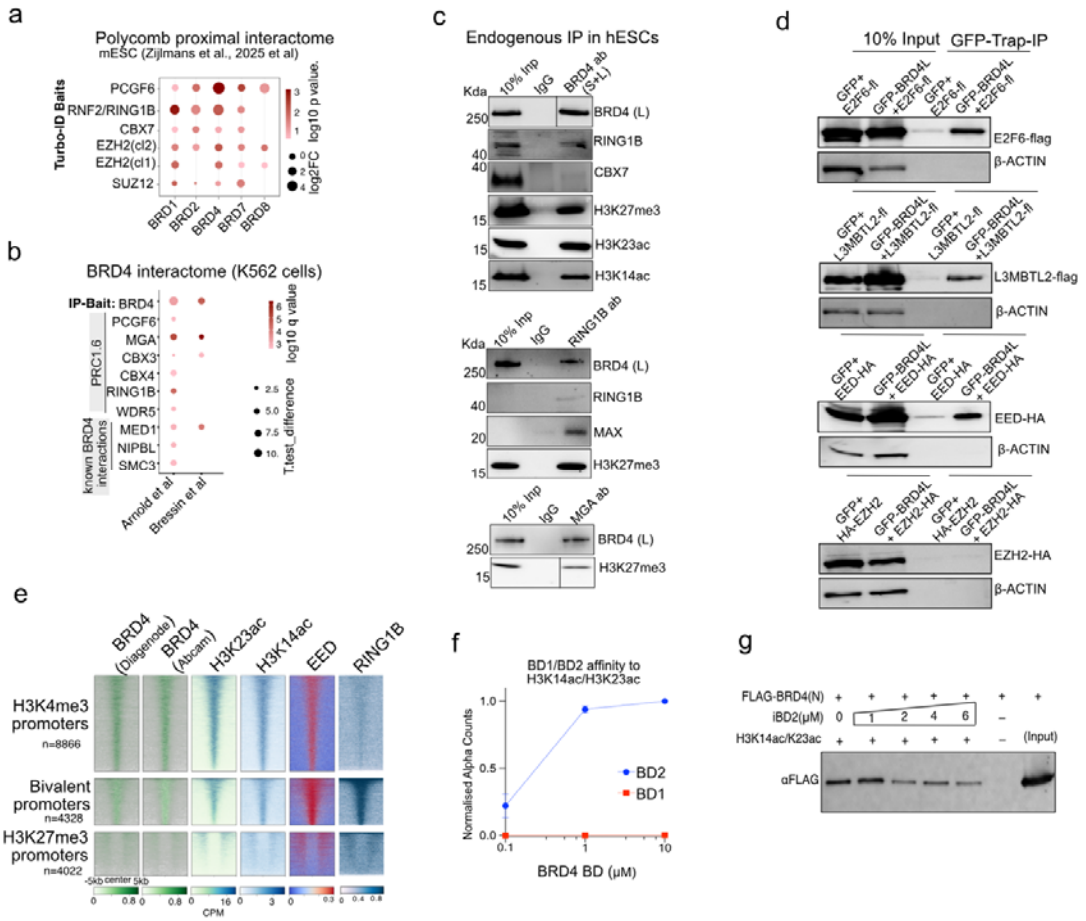

Figure 3. BRD4 interacts with PRC1.6, PRC2 proteins and H3K14ac/H3K23ac. a) Dot plots showing log2 fold enrichment of BRD proteins in the proximal interactome (Turbo-ID) for PRC1 and PRC2 proteins from mouse embryonic stem cells (mESCs), data from [27]. The size of the circle represents the log2 fold enrichment in BRD4 IP relative to IgG control. **b**) Like (a) but for enrichment of PRC proteins in BRD4 immunoprecipitation from K562 cells, data from [28,29]. The size of the circle represents the t-test difference between the BRD4 IP and the IgG control. **c)** Immunoblots of endogenous BRD4 IP in H9 hESCs using antibodies that recognise both short and long BRD4 isoforms, with antibodies detecting RING1B, CBX7, CBX4, H3K27ac, H3K23ac, H3K27me3, along with reverse IP with RING1B and MGA antibodies followed by immunoblots for BRD4 and H3K27me3. **d**) Immunoblots of GFP-trap co-immunoprecipitation of GFP-BRD4 long isoform (GFP-BRD4L) with Flag- tagged E2F6 and L3MBTL2, HA- tagged EED and EZH2. Immunoblots for β-ACTIN served as controls, **e**) Heatmap of CUT&Tag for BRD4, EED, H3K23ac and ChIP-seq data for H3K14ac and RING1B, at active (H3K4me3+), bivalent (H3K4me3+/H3K27me3+) and PRC2 repressed promoters (H3K27me3+). **f**) AlphaScreen counts titration of BRD4-BD1 and -BD2 interaction with H3K14ac/23ac showing that only BRD4-BD2 interacts with H3K14ac/23ac. Normalized average alpha counts of three replicates were set relative to the highest WT. **g)** Immunoblots of biotinylated H3K14/K23ac pulldown for N-terminal His-FLAG tagged BRD4 (N-terminal 412 amino acids), in the presence of increasing concentration of iBET-BD2 (iBD2).

BRD4 BD2 mutations lead to upregulation of developmental and neuronal genes

To determine the effect of BRD4-BD1 (N145G) and BRD4-BD2 (Y390C, Y430C) CdLS missense variants on the ability of recombinant BRD4 bromodomains to bind acetylated histone H3 and H4 tails, we performed AlphaScreen assays (Supplementary Fig. 4a-4c). All three BRD4 CdLS missense

variants reduced bromodomain binding to a tetra-acetylated H4 (H4K5/8/12/16ac) peptide. However, the binding of BRD4-BD2 Y430C to a diacetylated H3 peptide (H3K14ac/K23ac) was not impacted (Supplementary Fig. 4a-4c). These findings suggest that BRD4 bromodomain missense variants associated with CdLS might alter BRD4 genomic occupancy, as H4 and H3 acetylation modifications are differentially enriched at regulatory elements and at bivalent chromatin [30,33–35].

To investigate the impacts of BRD4-BD2 loss-of-function mutations on gene expression programmes in hESCs and in the neuronal lineage, we used CRISPR to generate H9 and H1 hESCs with a homozygous deletion of amino acid 429 ($BRD4^{C429\Delta}$, hereafter BRD4-BD2mut1) (Supplementary Fig. 4e and 4f). BRD4-BD2mut1 exhibited reduced occupancy across enhancers and promoters in hESCs (Fig. 4a). We found significant overlap in upregulated (n=1800) and downregulated (n=2502) genes between BD2mut1 and those upon 20 hours of dTAGV-1-mediated BRD4 degradation (Fig. 4b and 4c). These commonly upregulated genes are associated with neuronal cell proliferation and differentiation pathways (Figs. 4b and 4c). Furthermore, RNAseq performed after differentiation of BRD4-BD2mut1 and WT hESC clones into neurons revealed a significant upregulation of 672 bivalently marked genes in neurons (Figs. 4d-4f). These findings demonstrate that loss-of-function mutations in BRD4 can alter the expression of PRC-repressed bivalent genes in both stem cells and in the neuronal lineage.

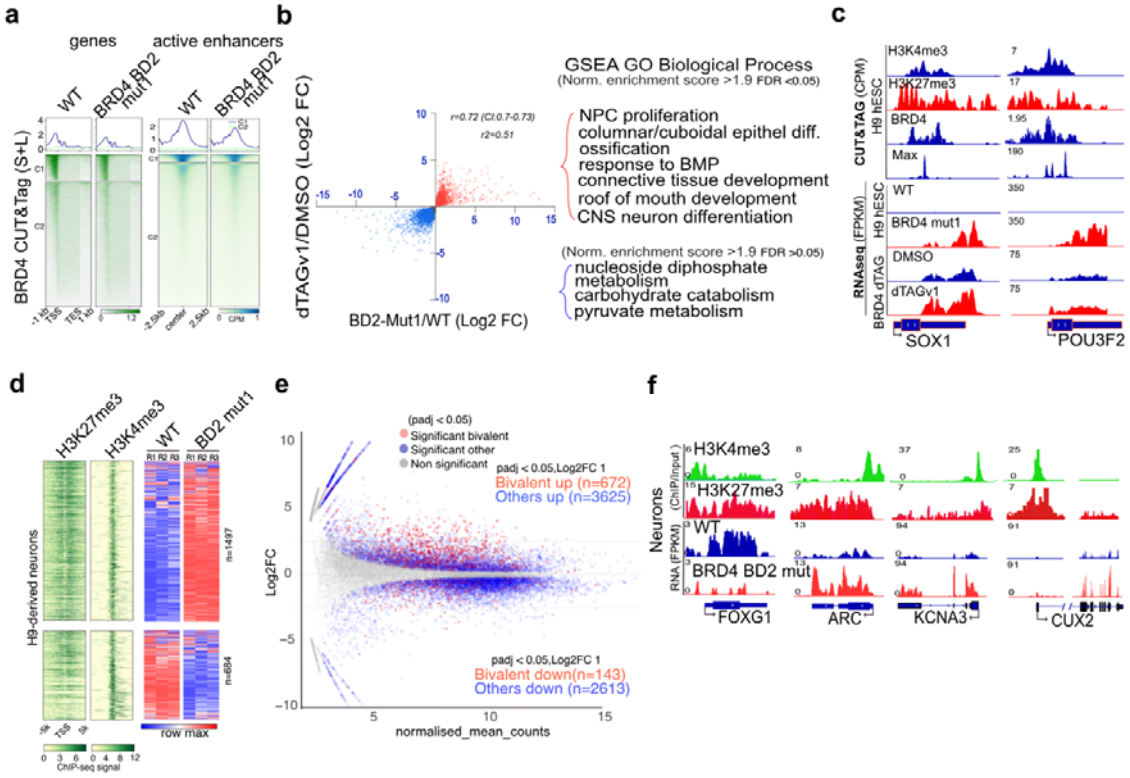

Figure 4: BRD4 BD2 mutations lead to upregulation of neuronal genes.

a) Heatmap showing BRD4 signal (CPM) for WT and BRD4 BD2 mut1 at protein-coding genes and active enhancers of hESCs. **b**) Scatter plot comparing log2 fold change (log2 FC) values for BRD4 BD2-Mut1/WT (X-axis) against BRD4 dTAG/DMSO (Y-axis) conditions. GSEA GO-biological process enrichment lists for genes that are commonly up (red) and down (blue) regulated in both conditions (right). **c**) Representative genome browser snapshot displaying signals for RNA-seq WT, BRD4-mutant1, DMSO and dTAGV-1 along with MAX, BRD4, H3K27me3 and H3K4me3. For CUT&Tag (BRD2,3,4, H3K4me3, H3K27me3) and CUT&Run (EED, ser5 Pol-II), the signal is

compared as CPM and MAX as ChIP-seq signal from ChIP-atlas. **d)** Heatmaps displaying H3K27me3 and H3K4me3 ChIP-seq signals along with RNA-seq normalized counts at bivalent genes in WT-H9 and H9-derived BRD4 BD2 mut1 neurons. **e**) MA plot illustrating differential gene expression in BRD4 BD2 mut1 compared to WT neurons. Significantly up- and down-regulated bivalent and non-bivalent genes are highlighted in red and blue, respectively. The number of differentially expressed genes with a log2 fold change of 1 and an adjusted p-value of <0.05 is indicated (right). **f**) Genome browser tracks showing ChIP-seq data for bivalent histone modifications (H3K4me3 and H3K27me3), fold change over input and RNA-seq (RPKM) for neuronal genes.

Acute BRD4 degradation leads to upregulation of neuronal genes in UNOs

We probed the roles of BRD4 in human embryonic brain development using UNOs derived from H1-hESCs using a well-established protocol [36,37]. Neurogenesis is known to begin at day 16 in UNOs and to reach highly divergent neuronal lineages around day 42, along with proliferating neural rosettes [38] (Figs. 5a and 5b). To identify genes regulated by BRD4 in neuronal cell populations, we performed bulk RNA-seq in UNOs treated with ZxH to induce acute BRD4 degradation. As in hESCs, acute BRD4 degradation led to upregulation of genes involved in synaptic, axonal, and neuronal projections, including several bivalently marked neuronal immediate-early genes (IEGs) (Figs. 5c-5e). These findings suggest that BRD4 and PRC proteins cooperate to maintain precise spatial and temporal control of genes involved in nervous system development and neural plasticity. They also likely play a key role in maintaining IEGs in a transcriptionally poised state, which is critical for rapid activation during the early stages of learning or memory formation [39,40].

BRD4 mutations lead to upregulation of neuronal and bivalent genes and altered cell fate

We next investigated the effects of heterozygous BRD4 loss-of-function mutations (to mimic de novo variants in CdLS patients) on diverse neuronal cell populations in UNOs as an in vitro embryonic brain development model. For this purpose, we generated H1 hESC clones with two independent heterozygous BD2 mutants. One clone had an in-frame deletion of amino acids 425-430 in one allele ($BRD4^{425\text{-}430\Delta/WT}$, here on BRD4-BD2mut2) and the second clone had an in-frame deletion of amino acid 429 ($BRD4^{C429\Delta/WT}$, here on BRD4-BD2mut3), and an isogenic WT clone (Supplementary Fig. 5a). To investigate the effect of BRD4 mutations on neuronal cell fate and gene expression programme in proliferating neuronal stem cells and in multiple neuronal lineages, we generated scRNA-seq libraries for 41- and 63-day wild-type, BRD4-BD2mut2 and BRD4-BD2mut3 UNOs. To prevent batch effects during library preparation cells from WT and mutant UNOs were multiplexed by antibody-based barcoding at 41 and 63 days. We generated a total of six single-cell libraries totalling 11746 cells at day 41 and 10537 cells at day 63. We further employed the cluster similarity spectrum (CSS) to remove batch effects between time points [41].

Dimensionality reduction and embedding of the scRNA-seq data using uniform manifold approximation and projection (UMAP) revealed diverse populations (Fig. 5f and Supplementary Figs. 5b-d) [42]. Annotation of clusters by comparing the expression of reference markers from each population (Supplementary Fig. 5d) revealed proliferating progenitors (G2M), Diencephalic progenitors, GABAergic and Glutamatergic lineage, as well as retinal pigment epithelium (RPE), and optic vesicle (Fig. 5f) [43,44]. Cell type composition analysis showed a reduced Diencephalic progenitor cell population 1, and an increased number of Diencephalic progenitor cell cluster 2, optic vesicle and RPE cells in the two mutant organoids (Fig. 5f and 5g). This is consistent with the appearance of RPE-like pigmentation in mutant, but not in WT UNOs at day 41 (Fig. 5h). We found enrichment of HOX and ZIC gene families that are known to be regulated by polycomb complexes among genes that are consistently upregulated in both BRD4 mutant UNOs (Supplementary Fig. 6a). It is worth noting

that several tested genes upregulated in BRD4 BD2 mutant UNOs are upregulated upon acute BRD4 degradation in UNOs.

We then asked whether genes that are upregulated in UNOs with heterozygous BRD4 BD2 mutations are enriched for bivalent modifications. We used publicly available single-cell CUT&Tag (scCUT&Tag) data for H4K4me3, H3K27me3, and H3K27ac from 35-, 60-, and 120-day-old UNOs to generate a list of bivalent chromatin regions in neuronal lineages [44]. Some of these upregulated genes harbour bivalent modifications (Fig. 5i and Supplementary Fig. 6b). Many of these genes are marked with H3K4me3 but lack detectable H3K27me3. The BRD4-PRC1.6 axis likely mediates repression of these genes, as the PRC1.6 complex is known to occupy and repress genes independently of PRC2 [26], consistent with the occupancy of BRD4 and PRC1.6 at active genes in hESCs (Fig. 2). We found that several key developmental TFs, such as ZIC and HOX family genes, which are bivalently marked, are upregulated in G2M cells and in the Glutamatergic lineage (Fig 5i). Transcription factor families known to play key roles in normal brain development and neuronal cell proliferation and specification (*e.g.*, ZIC, HOX) are upregulated in neuronal cell types in BRD4-BD2 mutant UNOs (Supplementary Figs. 6a and 6b). Taken together, our results indicate that BRD4 BD2 mutations can deregulate PRC-repressed genes in neuronal cell types.

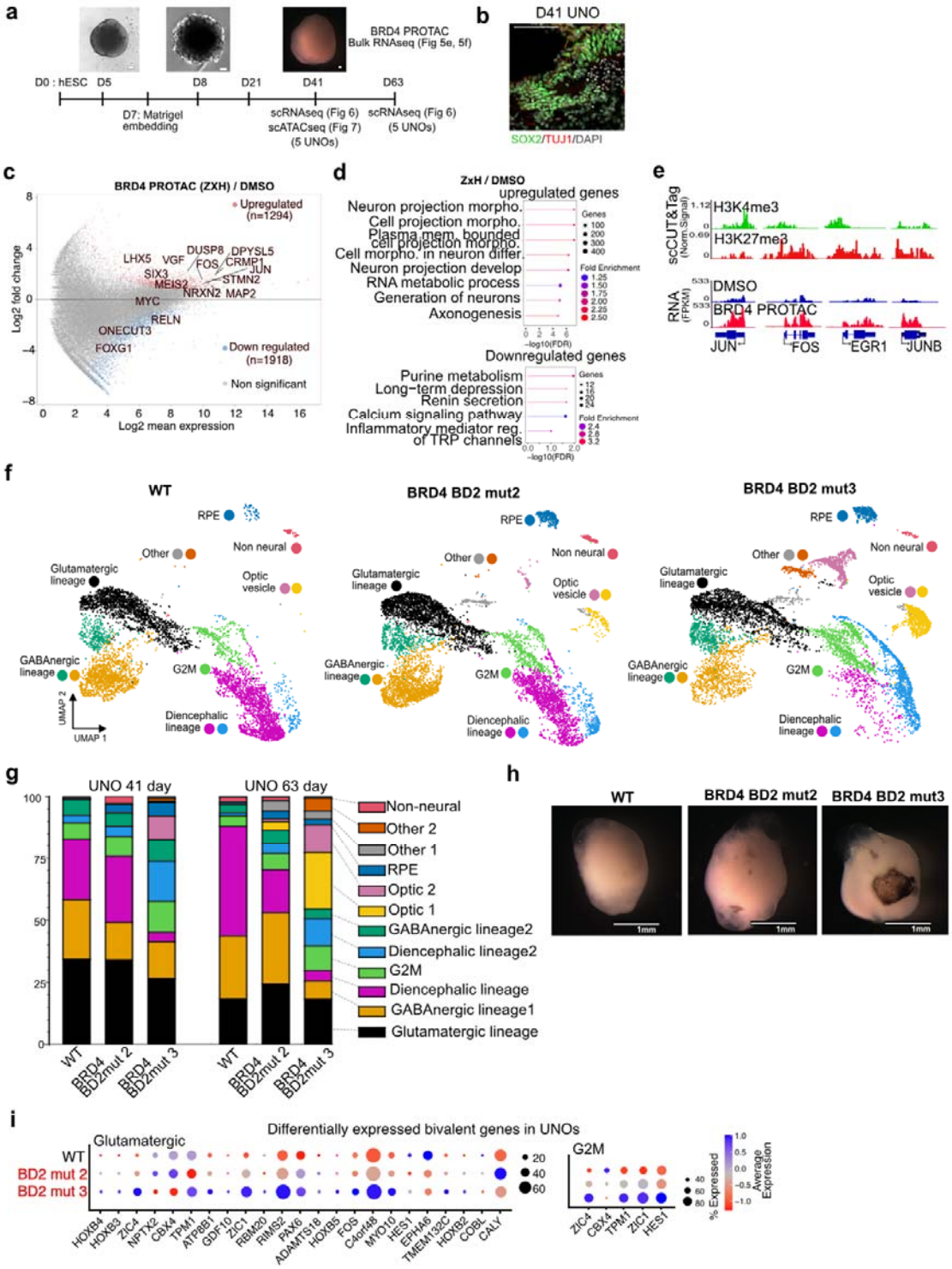

Figure 5. BRD4 BD2 mutations lead to deregulation of bivalent genes and altered cell fate in UNOs. a) Schematic representation of the protocol used to generate unguided neuronal organoids (UNOs), with images of UNO WT at 5,8, and 41 days. **b**) Immunofluorescence images of UNOs at day 41 stained for markers of neuronal progenitor (SOX2), post-mitotic early neurons (TUJ1), scale bars: 100 µm. **c**) MA plot for RNA-seq data illustrating differentially expressed genes in day 41 UNOs following 20 hours of BRD4 PROTAC (ZxH) treatment (n=3 independent organoids). **d)** Gene

ontology (GO) enrichment analyses of up- and down-regulated genes. **e**) Genome browser tracks for normalized reads at TSS for pseudo bulk scCUT&Tag and bulk RNA-seq for immediate early genes (IEGs) upon 20 h BRD4 PROTAC in UNOs (data from (c)). **f)** UMAP plots stratified by genotype show the annotated cell lineages: WT, *BRD4* BD2 mut2, and *BRD4* BD2 mut3. Cell clusters are identified by colour, illustrating the contribution of each genotype to specific lineages, such as Glutamatergic, GABAnergic, optic vesicle, and RPE. **g)** Stacked bar charts for 41-day and 63-day UNOs, detailing the percentage of cells for each annotated cell type across the WT, *BRD4* BD2 mut2, and *BRD4* BD2 mut3 UNOs. **h)** Representative bright-field microscopy images of 41-day UNOs, Scale bar=1mm (rest of the images in source file). **i)** Dot plots showing the average expression level (Z scores) and percentage of cells expressed in Glutamatergic, Diencephalic-1(pink in UMAP), and Diencephalic-2(blue in UMAP), and G2M clusters for bivalent genes that showed significant differential expression in the scRNA-seq data in BRD4-BD2 mut1 and BRD4-BD2 mut2 UNOs.

Upregulated transcription factor families lead to an altered chromatin accessibility landscape in neuronal cells

To investigate the chromatin accessibility landscape of the altered gene regulatory network in BRD4 BD2 mutant UNOs, we conducted single-cell ATAC-seq (scATAC-seq) on day 41 UNOs, which resulted in 4236 WT and 4103 BRD4 mut2 scATAC-seq libraries. Consistent with the increased proportions of Diencephalic populations and RPE genes in our scRNA-seq analyses, scATAC-seq data showed a similar increase in these populations (Fig. 6a and Supplementary Figs. 7a and 7b). TF motif enrichment analysis of scATAC-seq peaks gained in BRD4-BD2mut2 UNOs indicated that many TF families are enriched, including the C_2H_2 zinc finger (C_2H_2ZNF) family, Homeodomain TFs, and bZIP TFs, which are involved in brain development and cognition (Fig. 6b) [45,46]. This is consistent with the upregulation of bZIP TFs such as JUN, FOS, and EGR1; Homeodomain TFs such as HOXB2; and C_2H_2ZNF TFs such as ZIC1 and ZIC4 (Fig. 5i and Supplementary Figs. 6a and 6b). These findings suggest that upregulation of TF families regulated by BRD4 and the polycomb axis could contribute to increased chromatin accessibility and transcriptional activation (Fig. 6b and Supplementary Fig. 7c). We also found cluster-specific and central enrichment of TF motifs at the scATACseq peaks that gain in BRD4 mutant UNOs (Fig. 6b and Supplementary Fig. 7c). For example, regions open in the Diencephalic cluster are enriched for bZIP and Homeodomain families; Glutamatergic clusters are enriched for T-box and bHLH motifs; GABAnergic clusters are enriched for Homeodomain-POU factors; and G2M clusters are enriched for bZIP and SOX factors (Fig. 6b). Notably, the MGA/MAX heterodimer binds T-box and bHLH motifs[47], validating that BRD4 perturbation de-represses genes bound by MGA/MAX TFs which are known to recruit PRC1.6.

Many bivalently marked genes in the developing brain, such as those in the ZIC, PAX, SOX, and HOX families of transcription factors, are consistently upregulated following acute BRD4 degradation and loss-of-function mutations. Upregulation of these TFs, which are vital for CNS development and function, coincides with increased accessibility of their specific motifs (Fig. 6b, Supplementary Fig. 7c). These findings suggest that BRD4, in complex with polycomb proteins, plays a vital role in regulating the transcriptional landscape underlying neuronal lineage specification, patterning, and learning and memory formation. Our findings emphasize the crucial role of the key epigenetic regulator BRD4 in preventing the premature activation of developmental genes, thereby maintaining a delicate balance between cell identity and differentiation.

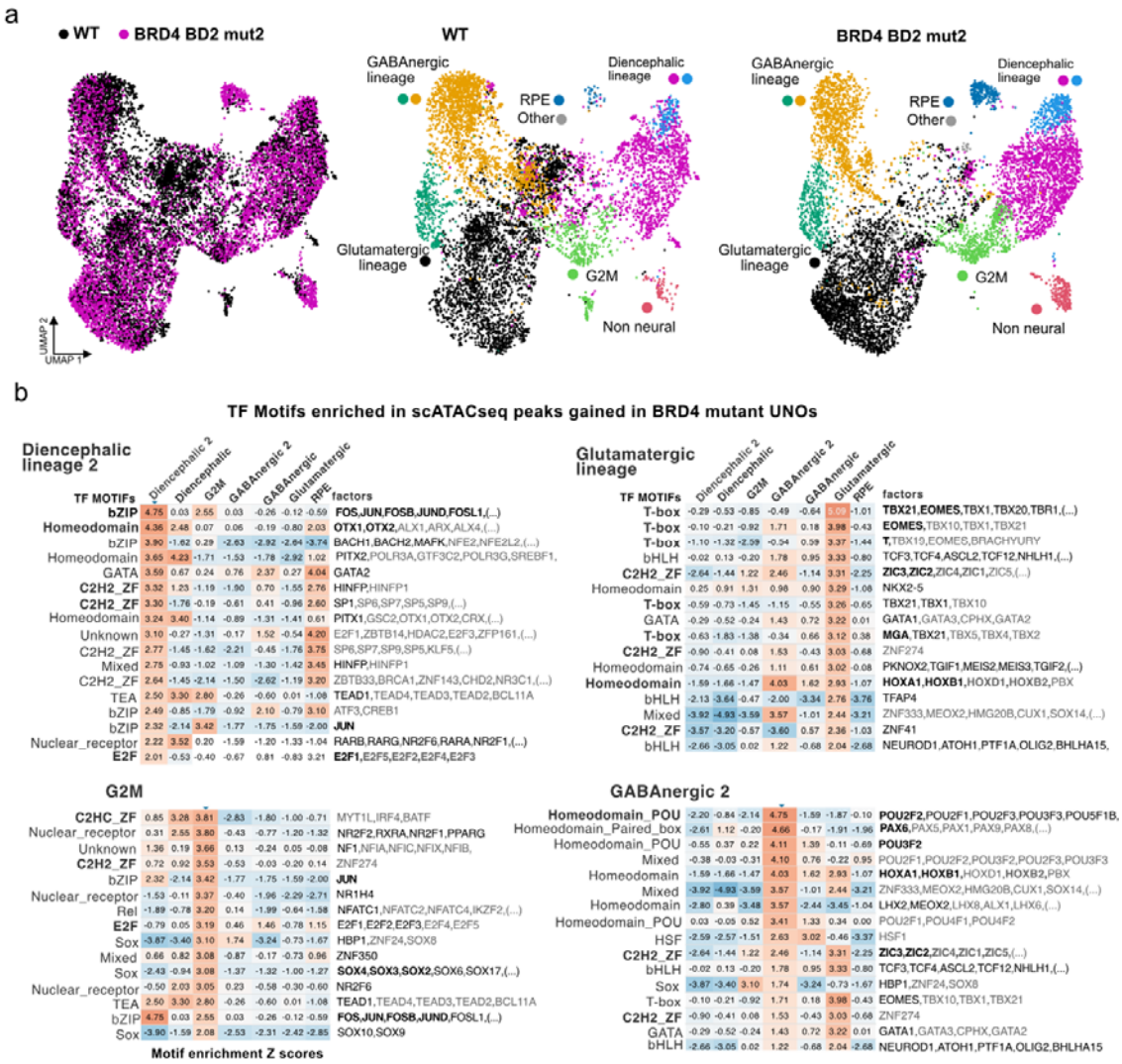

Figure 6: scRNAseq and scATACseq show altered levels of neuronal TF genes BRD4 mutant UNOs. a)UMAP plots show the distribution of single-cell ATAC sequencing (scATAC-seq) data clustered by genotypes WT and *BRD4* BD2 mut2 and annotated by cell lineage for WT and *BRD4* BD2 mut2. **b**) Z-scores (high scores in red and low scores are in blue) showing top transcription factor motifs enriched at Diencephalic, Glutamatergic, G2M and GABAnergic lineages across scATACseq peaks, which are gained in BRD4 BD2 mut 2 UNO compared to WT control. The complete list of enriched TFs is in the source data table.

Discussion

We have identified that the epigenetic regulator protein BRD4 maintains the repressive or poised state of developmental genes by binding to bivalently marked promoters through its bromodomains, which recognize H3K14ac and H3K23ac. These repressive roles are mediated by interactions with components of the PRC2 and noncanonical PRC1.6 complexes. BRD4 plays a context-specific role in mediating the choice between transcriptional activation and repression, balancing cell identity and differentiation by repressing bivalently marked developmental and neuronal genes in ESCs and in the neuronal lineage.

BRD4 interacts with PRC1.6 at active and bivalently marked promoters and represses developmental genes

BRD4 co-occupies with PRC1.6 components at active and bivalent promoters, consistent with findings that PRC1.6 is among the most abundant forms of PRC1 complexes in ESCs, where it plays a key role in repressing genes independently of both H2Aub and H3K27me3 [48,49]. PRC1.6 is associated with various accessory subunits, such as the MGA/MAX heterodimer, which provides affinity for T-box motifs. TF motif enrichment in scATAC-seq data suggests that loss-of-function mutations in BRD4 could affect MGA-mediated repression of target genes regulated by T-box motifs. Although MGA is crucial for embryonic development, a recent report indicates that *de novo MGA* variants are linked to developmental, ocular, and congenital anomalies [50]. The interaction between BRD4 and the PRC1.6 complex, and the upregulation of PCGF6 and MGA target genes upon BRD4 degradation, support a role for BRD4 in PRC1.6-mediated repression.

Role of H3K14/K23ac in recruiting BRD4 to PRC-regulated regions

Although PRC-repressed chromatin is depleted of H3K27ac, these chromatin regions are enriched with histone acetylations such as H3K9ac, H3K14ac, H3K23ac and H3K122ac [23,30,34,51]. Here, we show enrichment of BRD4 at H3K14ac/H3K23ac/H3K27me3 at polycomb-regulated bivalent genes and specific affinity of BRD4 BD2 to H3K14ac/H3K23ac peptides in vitro. These findings are consistent with large-scale proteomics analysis of modified-nucleosome pulldown data, which showed that BRD4 binds to combinations of H3K18ac/H3K27me3 and H3K23ac/H3K27me3 [52]. Interestingly, our data show that the BD2 inhibitor reduces the interaction between BRD4 and H3K14/23ac, suggesting that use of this specific BD2 inhibitor could alter BRD4 occupancy. Since BRD4 occupancy overlaps with MAX/MGA sites and H3K14/23ac nucleosomes, we propose that BRD4 could be recruited to PRC1.6 and bivalent chromatin through multiple mechanisms. Future studies should test whether MAX/MGA contribute to recruiting BRD4 to PRC1.6-regulated genes or vice versa.

BRD4 BD2 mutations lead to altered expression of genes involved in neuronal development

Patients with BRD4 variants do not display the typical CdLS phenotype, which includes characteristic facial features, growth failure, hypertrichosis of the face and other areas, and radial or limb anomalies [16]. However, most patients with BRD4 variants exhibit microcephaly, learning difficulties, intellectual disability, and a global developmental delay phenotype [16,53], indicative of nervous system disruptions. BET bromodomain inhibitors and shRNA-mediated depletion of BET proteins in mouse neural progenitor cells (NPCs) [54]. The inhibition of BET proteins in a *Xenopus* developmental model also alters pluripotency and neural crest formation [55]. Similarly, BRD4 depletion also disrupts neural crest differentiation in the mouse model [4]. The upregulation of many bivalently marked TFs, such as RIMS2, ONECUT1, SIX3, and PAX6, which are essential for retinal cell differentiation, and the increased composition of retinal and cell types, suggest that the loss of BRD4 increases differentiation of Diencephalic progenitors shifted towards retinal cell fates in our UNOs (Figure 5). These altered differentiation trajectories are consistent with developmental phenotypes observed in the heterozygous BRD4 knockout mouse model, which exhibits significant craniofacial, neurological, and vision/eye-associated defects, including decreased retinal thickness [56]. This corroborates the common occurrence of cataracts and other ophthalmological manifestations commonly observed in CdLS cases [53,57]. Overall, these findings demonstrate that deregulation of developmental and neuronal genes caused by mutations in key epigenetic regulators, such as BRD4, contributes to neurodevelopmental disorders.

Mutations in regulators of histone acetylation and PRCs lead to NDDs

Variants in genes encoding components of chromatin regulatory complexes that alter H3K4me3 levels at bivalent sites, PRC repressor proteins, and genes that alter PRC modification levels (H2A119ub and H3K27me3) are implicated in many NDDs (*e.g.*, Weaver syndrome, Kabuki syndrome, Cohen-Gibson syndrome) with common phenotypes including macrocephaly, intellectual disability, and craniofacial and skeletal abnormalities [58–61]. PRC1.6 and PRC2 regulate the balance between neuronal self-renewal and differentiation [25,62,63]. Although histone bivalency is known for its role in early embryonic development, bivalent chromatin is also a highly prevalent feature of central nervous system and brain development [44,64,65]. Indeed, many brain-specific TFs and genes that play key roles in specific neuronal lineages are bivalently marked chromatin regions [65], indicating that the bivalency of chromatin modifications mediates the precise regulation required for brain development and function. We show that loss-of-function mutations in BRD4 or its acute degradation lead to the deregulation of key developmental TF families, including HOX, ZIC, FOXG1, SOX, PAX, and SIX. Mutations in these gene families are known to cause various NDD phenotypes [66–70]. Therefore, many neurodevelopmental and craniofacial abnormalities observed in CdLS cases may stem from the brain-specific TF changes in gene expression and chromatin accessibility resulting from loss-of-function BRD4 variants.

The contributions of BRD4 to the positive regulation of gene expression through enhancer-mediated control and transcriptional elongation are well-known. Here, we have defined a novel role for BRD4 in transcriptional repression by modulating the accessibility and transcription of bivalent chromatin regions via interactions with acetylated histones and the PRC1.6 and PRC2 complexes. The knowledge gained from this study provides a foundation for future studies investigating the functional implications of BRD4 loss-of-function and the dysregulation of transcriptional repression in CdLS and other NDDs.

Methods

hESC culture

H9 (WiCell) and H1 hESCs (WiCell) were cultured in mTeSR+ (Stemcell Technologies Cat.# 100-0276) on Matrigel hESC-Qualified Matrix (Corning Cat.# 354277). Cells were split at a ratio of 1/10-1/20 with ReLeSR (Stemcell Technologies Cat.# 100-0484) or Accutase (ThermoFisher Scientific Cat.# 00-4555-56) if the experiment required single-cell splitting.

Cells were treated with 100 nM of BRD4 PROTAC (Cat. # T17297 ZxH-3-26) for 4 to 20h, 5 µM of KAT6/7 inhibitor (Cat.# HY-132283 PF9363) for 4h or 1 µM of iBET-BD2 (Cayman Chemical, Cat.# Cay31766-1) for 16h. Cell cultures were routinely tested for mycoplasma contamination by semi-quantitative PCR.

Generation of BRD4 mutant hESCs

We generated our BRD4 mutant hESCs from H9 and H1hESC. We designed gRNA targeting aa430 in the BD2 domain. We use the Nucleofector (Lonza, Nucleofector 4D) with programme number CB150. 0.2 million cells were nucleofected with an RNP complex containing Cas9 (IDT Cat# 1081060) and gRNA (AGGGTTGTACTTATAGCAGT), both from IDT, and P3 Primary Cell 4D Nucleofector X Kit (Lonza, Cat# V4XP-3032). Colonies were manually picked and then sequenced for genotyping.

Generation of BRD4 dTAG hESC line

We generated H9 hESC with a degron tag (FKBP) at the N-terminus of BRD4 by transfecting RNP containing Cas9 and gRNA targeting the N-terminus of BRD4, along with plasmids containing microhomology for the N-terminus of BRD4. H9 hESCs were nucleofected to H9 hESCs using the

Nucleofector 4D (Lonza, Nucleofector 4D with programme CB-150) device and P3 Primary Cell 4D Nucleofector X Kit (Lonza, Cat# V4XP-3032) with RNP containing CAS9 (IDT) and guideRNAs ATGTCTGCGGAGAGCGGCCC (targeting N-terminus of BRD4, IDT), and GCATCGTACGCGTACGTGTT (targeting PITCH, IDT) along with two BRD4 N-terminal dTAG constructs, one expressing puromycin resistance (pCRIS-PITChv2-dTAG-BRD4-puroR, Addgene Cat# 91793) and blasticidin resistance (pCRIS-PITChv2-dTAG-BRD4-blastiR, Addgene Cat# 91792). Plasmids were a gift from James Bradner and Behnam Nabet [22]. Targeted clones were selected with 0.5 mg/ml puromycin and 2.5 μg/ml blasticidin for 10 days, starting five days after nucleofection. Surviving colonies were genotyped by initial PCR and Sanger sequencing, and the edits were further confirmed by western blotting with an HA antibody (Thermo Fisher Scientific, Cat. #26183) to detect correctly edited BRD4; degradation efficiency was verified by treating them with dTAGV-1 and dTAG13.

NSC induction of hESCs and neuronal differentiation

Neural stem cells (NSCs) were derived from WT and BRD4 BD2 mutant H9 hESCs using the manufacturer's protocol (Life Technologies, MAN0008031) and expanded in neural expansion medium (NEM), which consisted of Neurobasal medium(Thermo Fisher; Cat.# 21103049) and advanced DMEM/F12 (Thermo Fisher; Cat.# 12634010). The media was supplemented with a neural induction supplement (Thermo Fisher; A1647801) and penicillin/streptomycin. NSCs were validated by immunolabelling and used for neuronal differentiation between passages 6 and 10. NSCs were differentiated into forebrain neurons using STEMdiff™ Forebrain Neuron Maturation Kit (Stem Cell Technologies, Cat. # 08605) for 21 days to produce a mixed population of excitatory and inhibitory forebrain-type neurons.

Unguided neural organoids (UNOs)

Unguided neural organoids were generated using the cerebral organoid kit (Stem Cell Technologies, Cat #08570). Briefly, 9000 cells were plated in a low attachment 96-well plate in EB seeding media, centrifuged for 3min at 400 × g, and then topped up with EB formation media on days 2 and 4. On day 5, they are transferred to induction media for 2 days. At day 7, embryoid bodies were embedded in 15 μL of Matrigel basement membrane matrix (Corning, Cat. #354230) and transferred to a low attachment 6-well plate in expansion media. After 3 days in expansion media, they were transferred to maturation media on an orbital shaker at 65 rpm.

For scRNA-seq and scATAC-seq, 5UNO samples were pooled and processed using a papain-based dissociation kit (MACS, Miltenyi Biotech, Cat. # 130-092-628). Briefly, UNOs were cut in half with a scalpel blade and processed with 2 mL of preheated papain solution for 15 minutes at 37 °C. The enzyme mix was added to the UNO pieces, and was triturated with wide-bore p1000 and regular p1000 pipette tips. They were incubated twice for 10 minutes at 37 °C, with trituration steps in between, using p200 and p1000 pipette tips. Cells were filtered with 30 μm filters, centrifuged, and processed for scRNA-seq and scATAC-seq library preparation using 10x scRNA-seq Chromium Next GEM Single Cell 3 Kit (10x Genomics, Cat.# PN-1000121) and 10x Chromium scATAC-seq Chromium Next GEM Single Cell ATAC v2 kit (10x Genomics, Cat.# PN-1000390). UNOs at days 41 and 63 were processed separately: cells were dissociated from WT and two mutant UNOs, which were labelled with antibody-based hashtag oligos (HTOs), and pooled before loading onto a 10x Genomics chip.

Immunofluorescence on UNOs

UNOs were fixed in 4% paraformaldehyde at 4°C overnight, washed 3 times with PBS, embedded in OCT after a sucrose gradient, and frozen at –80 °C. Sections were cut with a cryostat LEICA

CM1850 at 20μm and placed on microscope slides (Epredia, Cat# J1800AMNZ). Sections were washed with PBS, permeabilized using 0.15%Triton X-100, blocked using 0.15%Triton X-100/2%BSA for 1h, and incubated at 4 °C overnight with primary antibodies anti-SOX2 (Santa Cruz Biotechnology, Cat# sc-365964, 1/1000) and anti-TUJ1 (BioLegend, Cat# 802001, 1/1000). After washing with PBS-0.15 % Triton X-100 three times, the sections were incubated with secondary antibodies conjugated to different fluorophores and DAPI for 2h at RT, then washed with PBS-0.15 % Triton X-100 and mounted with Dako mounting medium. Sections were imaged with a Zeiss LSM 800 confocal microscope.

Proximity Ligation Assay (PLA)

WT and BRD4 mutant hESCs were seeded in glass-bottom 96-well plates. PLA was performed using the Duolink In Situ Red Starter kit (Mouse/Rabbit) according to the manufacturer's protocol (Merck, DUO92101) and permeabilized using 0.1% Triton-X-100 for 5min. Antibodies anti-BRD4 (Abcam, Cat.# ab244221, 1/200), anti-H3K27ac (Abcam, Cat. # ab4729, 1/800), anti-H3K27me3 (Cat. # 07-449, 1/500) and anti-H3K23ac (Cat.# 07-355, 1/500) were used. Plates were imaged in the laser-based InCell high-content imaging system (IN Cell Analyser 6000, GE Healthcare). The images were analyzed using dedicated software, INCarta. The data used for comparison are listed in Supplementary Data 1.

Bulk RNA-seq in WT and BD2 mutant hESC, and neurons

For WT and BD2 mutant H9 hESCs, NPCs and neurons, total RNA was isolated using NEB Monarch kits; ribosomal RNAs were depleted using the RiboCop kit (Lexogen, Cat.# 144), RNA-seq libraries were generated using the CORALL total RNA-seq V2 kit (Lexogen Cat.# 183) followed by sequencing as 150bp paired-end reads.

Bulk RNA-seq upon dTAG and PROTAC treatment

RNA-seq libraries upon BRD4 PROTAC (TargetMol Chemicals, Cat. # T17297, ZxH-3-26) in H9 hESCs, and dTAGV-1 treatment in H9 hESC-BRD4-dTAG lines were generated using NEBNext® Poly(A) mRNA Magnetic Isolation Module (NEB, Cat.# E7490L) followed by NEBNext® Ultra™ II RNA (NEB, Cat.# E7770L).

Endogenous Immunoprecipitation

Cells were lysed in native IP buffer (20 mM Tris, pH 8.0, 50 mM NaCl, 0.5% (vol/vol) IGEPAL CA-630, 10% (vol/vol) glycerol) containing protease and phosphatase inhibitors, and incubated on ice for 4 min. Nuclei are centrifuged at 15500 × *g* for 10 min, then resuspended in native IP buffer + Benzonase (Millipore Sigma, Cat.# 707463 final concentration, 1.25 U/μl) for 30 min on ice. Extracts were cleared by centrifugation at 15500 *g* for 10 min at 4°C. The supernatant was precleared with Dynabeads A bead on ice for 5min. The precleared extract was then rotated with 1 μg of antibodies anti-BRD4 (Cell Signalling, Cat. # 83375), anti-RING1B (Active Motif, Cat. # 39663), anti-MGA (Antibodies Online, Cat.# ABIN2444597) or IGG (ThermoFisher Scientific, Cat. # 500-P00-500UG) for 2 hours at 4 °C before adding the Dynabeads A bead for 30min at 4 °C. After two washes in native IP buffer and three more in IP washing buffer (20 mM Tris, pH 8.0, 125 mM NaCl, 0.5% (vol/vol) IGEPAL CA-630 and protease inhibitors), bound proteins were eluted by heating the beads with 1× Bolt sodium dodecyl sulphate (SDS) loading buffer, and separated on a Bolt™ Bis-Tris Plus, transferred to a nitrocellulose membrane, and immunoblotted with primary antibodies anti-BRD4 (Santa Cruz Biotechnology, Cat. # sc-518158), anti-BRD3 (Active Motif, Cat. # 61489), anti-H3 (Diagenode, Cat. # C15210011), anti-RING1B (Active Motif, Cat. # 39663), anti-CBX7 (Abcam, Cat.# ab21873), anti-MAX(,), anti-ACTb (Abcam, Cat.# ab8226), anti-H3K27me3 (Millipore, Cat.#

07-449), anti-H3K23ac (Millipore, Cat.# 07-355) and H3K14ac (Active Motif, Cat.# 65701) overnight at 4°C or 1 hour at room temperature on a nutator. After three washes with PBST, membranes were incubated with fluorescence secondary antibodies (StarBright™ Blue 520 Goat Anti-Mouse IgG BioRad Cat. # 12005867, StarBright Blue 700 Goat Anti-Rabbit IgG, BioRad, Cat. # 12004162 and DyLight 800 Anti-Mouse IgM ThermoFisher Scientific Cat. # SA510156) or HRP secondaries antibodies (TidyBlot BioRad Cat. # STAR209PT and Anti-Mouse IgM Invitrogen Cat. # 31440) and Anti-ACTIN hFAB™ Rhodamine Antibody BioRad, Cat. # 12004164). After three washes with PBST, the membranes were imaged using a BioRad imager.

Co-immunoprecipitation (Co-IP)

Co-IP was performed using the GFP-trap kit according to the manufacturer's protocol (ChromoTek GFP-Trap® Agarose kit, Cat # gtak), with modifications described below. ~1.2 million HEK293T cells were reverse transfected with 1ug of long isoform of GFP-BRD4 (Addgene 65378)[71] or pEGFP (Clontech**)** plasmids along with 1μg of pCMV-HA-hEZH2 (Addgene # 24230), pCMV-HA-EED (Addgene # 24231)[72], pcDNA3-FLAG-E2F6 (Addgene 236441)[73], pCMV-FLAG-hL3MBTL2 (Addgene # 28232)75 in 6 well plates using Lipofectamine 3000 reagent (ThermoFisher, Cat# L3000015). 24 hours after transfection, cells were lysed using 200 μl of RIPA lysis buffer (10 mM Tris/Cl pH 7.5, 150 mM NaCl, 0.5 mM EDTA, 0.1 % SDS, 1 % Triton™ X-100, 1 % deoxycholate, 0.09 % sodium azide, supplemented with Benzonase, proteinase inhibitor cocktail and PMSF) for 1 hour, lysate was cleared by centrifugation at 17000xg, supernatant was mixed with 300 μl of dilution buffer (10 mM Tris/Cl pH 7.5, 150 mM NaCl, 0.5 mM EDTA, 0.018 % sodium azide, proteinase inhibitor cocktail and PMSF). After saving 10% of the lysate for input, 450 ul of lysate is incubated with 15 μl of GFP-trap Agarose beads equilibrated in dilution buffer in an end-to-end rotor at 4 °C for 1 hour. Beads were washed with wash buffer (10 mM Tris/Cl pH 7.5, 150 mM NaCl, 0.05 % Nonidet™ P40 Substitute, 0.5 mM EDTA, 0.018 % sodium azide) and eluted by heating samples at 95C for 7 min in 1× Bolt sodium dodecyl sulphate (SDS) loading buffer, and separated on a Bolt™ Bis-Tris Plus, transferred to a nitrocellulose membrane, and immunoblotted with anti-Flag (Sigma Aldrich Cat# F7425) or anti HA (Proteintech Cat# 51064-2-AP) antibodies for overnight at 4C. After three washes with PBST, membranes were incubated with fluorescence secondary antibodies (StarBright Blue 700 Goat Anti-Rabbit IgG, BioRad, Cat. # 12004162 and Anti-ACTIN hFAB™ Rhodamine Antibody BioRad, Cat. # 12004164). After three 5-minute washes with PBST, the membranes were imaged using a BioRad imager.

Histone peptide pulldown

1 μg of biotinylated histone H3K14ac/H3K23ac peptide (Cayman Chemicals, Cat. 27520-250ug-CAY) was incubated with 10 μL of streptavidin magnetic beads (Invitrogen 656-01) in 300 μL of binding buffer (50 mM Tris, pH 7.5, 200 mM NaCl and 0.1% NP-40, proteinase inhibitor cocktail) and rotated at room temperature for 30 min. At the same time, FLAG-His tagged BRD4 *N*-terminal domain containing BD1 and BD2 (E49-E460) (MedChemExpress Cat# HY-P7846), inhibitor of iBET-BD2 (Cayman Chemical Cat# CAY31766), or DMSO were added to the binding buffer on ice. Biotinylated H3K14ac/K23ac peptide-bound streptavidin beads were added to the BRD4 in binding buffer and incubated overnight at 4 °C with rotation. The beads were washed with 1 mL of cold binding buffer 3 times with 3 min rotation each. Beads were resuspended in 30 μL of 1x Bolt sample loading buffer and heated at 95 °C for 5 min, then separated proteins using Bolt™ Bis-Tris Plus gels. Followed by western blotting using anti-FLAG antibody to detect BRD4.

CUT&Run

CUT&Run was performed according to 74 with modifications from the EpiCypher® CUTANA™ CUT&Run Protocol, pAG-Mnase from Epicypher (Cat. # SKU: 15-1116), and Cell Signalling Technology (Cat. # 403665). CUT&Run was performed using 500,000 cells. CUT&Run libraries are prepared using the NEBNext® Ultra™ II DNA Library Prep Kit for Illumina (Cat # E7645L) by following the protocol version 2 of the protocol.io approach adapted for CUT&Run library sequencing (dx.doi.org/10.17504/protocols.io.bagaibse). Primary antibodies used were anti-RAD21 (Abcam, Cat.#ab217678), anti-EED (Proteintech, Cat.# 16818-1-AP), anti-NIPBL (Bethyl, Cat.# A301-778A), anti-Phospho-Rpb1 CTD (Ser5) (Cell Signaling Technology, Cat.# 13523), anti-H3K27me3 (Diagenode, Cat.# C15410195), anti-BRD2 (Abcam, Cat.# ab139690), anti-BRD3 (Active Motif, Cat.# 61489), anti-H3K4me3 (Millipore, Cat.# 07-473).

CUT&Tag

CUT&Tag was performed according to the [76] protocol with modifications to tissue processing as described below. Experiments were performed in biological duplicates from each cell type. ~50,000 cells were pelleted by centrifugation for 3 min at 600 x g at room temperature and resuspended in 500µl of ice-cold NE1 buffer (20 mM HEPES-KOH pH 7.9, 10 mM KCl, 0.5 mM spermidine, 1% Triton X-100, and 20 % glycerol and cOmplete EDTA-free protease inhibitor tablet) and were let to sit for 10 min on ice. Nuclei were pelleted by centrifugation for 4 min at 1300 x g at 4°C, resuspended in 500 µl of wash buffer, and held on ice until the beads were ready. The required amount of BioMag Plus Concanavalin-A-conjugated magnetic beads (Polysciences, Cat.# 86057) was transferred into the binding buffer (20 mM HEPES-KOH pH 7.9, 10 mM KCl, 1mM CaCl2 and 1mM MnCl2), washed once in the same buffer, each time placing them on a magnetic rack to allow the beads to separate from the buffer and resuspended in binding buffer. 10 µl of beads was added to each tube containing cells, and the tubes were rotated on an end-to-end rotator for 10 minutes. After a pulse spin to remove liquid from the cap, the tubes were placed on a magnet stand to clear the liquid. The liquid was then withdrawn, and 800 µl of antibody buffer containing 1 µg of primary antibodies was added and incubated at 4 ºC overnight in a nutator. Primary antibodies used were anti-BRD4 (Diagenode, Cat.# C15410337), anti-BRD4 (Abcam, Cat.# ab128874), anti-H3K27ac (Abcam, Cat.# ab4729), anti-H3K9me3 (Diagenode, Cat.# C15410193) and H3K23ac (Millipore, Cat.# 07-355). Secondary antibodies (guinea pig α-rabbit antibody, Antibodies online, Cat.# ABIN101961) were diluted 1:100 in dig-wash buffer (5% digitonin in wash buffer), and 100 µL was added to each sample while gently vortexing to dislodge the beads from the sides, then incubated for 60 min on a nutator. Unbound antibodies were washed three times with 1 mL of dig-wash buffer. 100 µl of (1:250 diluted) protein-A-Tn5 loaded with adapters in dig-300 buffer (20 mM HEPES pH 7.5, 300 mM NaCl, 0.5 mM spermidine with Roche cOmplete EDTA-free protease inhibitor) was added to the samples, placed on a nutator for 1 hour and washed three times in 1 ml of dig-300 buffer to remove unbound pA-Tn5. 300 µL tagmentation buffer (Dig-300 buffer + 5 mM MgCl2) was added while gently vortexing, and samples were incubated at 37ºC for 1 hr. Tagmentation was stopped by adding 10 µL of 0.5 M EDTA, 3µL of 10% SDS, and 2.5 µL of 20 mg/mL Proteinase K to each sample. Samples were mixed by full-speed vortexing for ~2 seconds and incubated for 1 hr at 55ºC to digest proteins. DNA was purified by phenol: chloroform extraction using phase-lock tubes (Quanta Bio) followed by ethanol precipitation. Libraries were prepared using NEBNext HiFi 2x PCR Master mix (M0541S) with a 72ºC gap-filling step followed by 13 cycles of PCR with 10-second combined annealing and extension to enrich short DNA fragments. Libraries were sequenced on a Novaseq 6000 (Novogene) with 150 bp paired-end reads.

Analysis of CUT&Tag and CUT&Run data

For the CUT&Tag and CUT&Run, 150bp pair-end reads were pre-processed using Trimgalore with Fastqc, followed by local aligning to the hg38 genome using bowtie2[77], with the following pair-end parameters: –very-sensitive-local–no-unal–no-mixed–no-discordant–phred33 -I 10 -X 700. Mapping statistics are listed in Supplementary Data1 (Mapping statistics for NGS data). Mapped bam files were sorted and indexed using samtools [78]. For peak calling, the bedgraphs were generated using the SEACR pipeline[79]. Bigwig signal files as CPM were generated using the deepTools bamCoverage tool with CPM normalization, along with *–binSize 20 –normalize, using BPM or CPM–scaleFactor = 1.0–smoothLength 60–extendReads 150–centerReads* options. All CUT&Tag or CUT&Run were performed for at least two replicates. For replicates, the data were merged at the BAM level with samtools, followed by a similar processing pipeline to generate bigwigs or bedgraph files. Peaks were called using SEACR with options stringent 0.05 cutoff. CUT&Tag or CUT&Run heatmaps were plotted using the plotHeatmap function in deepTools on the matrix obtained from the computeMatrix output. Peak overlaps for the BRD4 peaks across publicly available ChIP-seq datasets were performed in the Cistrome-DB toolkit browser using the Transcription Factor option[80]. Peaks were overlapped using Intervene across multiple peak sets, including BRD4, E2F6, HDAC2, MAX, MYC, EED, RYBP, H3K14ac, H3K23ac, and H2A119Ub, and a correlation heatmap or upset plot was generated using the shiny version of Intervene. The enrichment of these peaks for ChromHMM states in H9 ESC was carried out using the peak2ann function from the genomation package in R. By calculating the overlap of BRD4 peaks on the 15 marks chromHMM states model (hg38 lifted) in H9-ESCs (E008) obtained from the Roadmaps epigenomics project.

Identification of Active, Bivalent, PRC1.6 target genes

To classify the genes as bivalent or active or PRC1.6 regulated, a heatmap for bivalent marks (H3K7me3 and H3K4me3), PRC1.6 marks (PCGF6, MYC, MAX, E2F6) and active marks (H3K27ac and H3K27ac) was compared along with EED, BRD2, BRD3, BRD4, H3K14ac and H3K23ac modifications in human ESCs. Clustering was performed to identify groups of genes based on the relative abundance of these modifications at the TSSs of protein-coding genes. Similar plotting was performed for bivalent active and H3K27me3-repressed promoters across human ESCs identified (data from [81]. Likewise, bivalent genes in H9-derived neurons were identified by plotting H3K27me3 (ENCFF285JOX) and H3K4me3 (ENCFF548EWT) signals.

Site-directed mutagenesis

His_6-tagged BRD4-BD1 (aa 57-168) and BRD4-BD2 (aa 333-460) constructs in the pNIC28-Bsa4 vector were gifts from Nicola Burgess-Brown (Addgene plasmid #38942 and #38943, respectively). Missense mutations in both bromodomains were generated by site-directed mutagenesis (GenScript) and confirmed by Sanger sequencing.

Protein purification

BRD4-BD1 WT, BRD4-BD1 N140A, BRD4-BD1 D145G, BRD4-BD2 WT, BRD4-BD2 Y390C, BRD4-BD2 Y430C, and BRD4-BD2 N433A were recombinantly purified from BL21(DE3) *E. coli* by nickel-affinity chromatography. BL21(DE3) cells were transformed and grown at 37 °C in 2XYT or Terrific Broth medium with 50 mg/L kanamycin to an optical density of 0.4-0.6 at 600 nm. Bacterial cultures were then grown at 18 °C to an optical density of 0.6-0.8 at 600 nm. Protein expression was then induced overnight with 0.1 mM IPTG at 18 °C. Cells were harvested *via* centrifugation at 5,000 rpm, and cell pellets were frozen at -80 °C until lysis. Frozen cells were thawed on ice and resuspended in lysis buffer (50 mM HEPES, 500 mM NaCl, 5% v/v glycerol, 5 mM imidazole, pH 7.5). 0.3 nM aprotinin, 1 nM E-64, 1 nM leupeptin, 1 nM bestatin, 1 nM pepstatin A, and 100 nM PMSF protease inhibitors were added to the lysis buffer used to resuspend frozen

cells, along with 5 µg/mL DNase I and 5 mM $MgCl_2$. Resuspended cells were immediately lysed via sonication for 10 minutes (pulsed, amplitude 3.5, 50% work cycle), and lysates were clarified by centrifugation for 30 minutes at 30,000 rpm. Clarified lysates were then applied to nickel-nitrilotriacetic acid (Ni-NTA) resin (~1 mL resin per L of culture) at 4 °C overnight while rocking. The protein-bound Ni-NTA resin was applied to a column and washed with 15 mL fractions of lysis buffer until nonspecific protein elution had ceased, as determined by monitoring the absorbance of the collected wash fractions at 280 nm. Protein was then eluted from the Ni-NTA resin using increasing concentrations of imidazole in lysis buffer (5 mL of 50, 100, 150, 200, and 250 mM imidazole). Fractions were resolved by SDS-PAGE, and those containing the BRD4 bromodomains of interest were pooled. BRD4-BD1 and -BD2 missense variants were dialyzed overnight in 6,000-8,000 Da molecular weight cutoff dialysis tubing (Fisher Scientific 08-670C) in 4L of storage buffer (50 mM HEPES, 500 mM NaCl, 5% v/v glycerol, pH 7.5), gently stirring at 4°C. BRD4-BD1 and -BD2 WT were further purified by gel filtration using an Enrich SEC 70 10 × 300 mm column (Bio-Rad) or a Superdex 75 Increase 10/300 GL column (Cytiva, 29148721) into storage buffer (50 mM HEPES, 500 mM NaCl, 5% v/v glycerol, pH 7.5). Monomeric protein was collected based on the chromatographs resulting from gel-filtration size-exclusion chromatography. Concentrations of all purified proteins were determined by the Bradford method using bovine serum albumin as a standard, aliquoted, flash-frozen, and stored at -80 °C.

AlphaScreen assays

All AlphaScreens were conducted in 96-well, ½ Area AlphaPlates (Revvity, 6002350) in a total volume of 40 µL. All stock solutions were prepared in AlphaScreen assay buffer, which consisted of 1x AlphaLISA Epigenetics buffer (Revvity, AL008F), 0.05% v/v Tween 20, and 2 µM tris(2-carboxyethyl)phosphine. Recombinant His_6-tagged BRD4-BD1 and BRD4-BD2 missense variants were assessed for the ability to bind to a biotinylated histone H3K14ac/23ac(1-27) peptide H_2N-ARTKQTARKSTGG-K(ac)-APRKQLAT-K(ac)-AGG-K(biotin)-COOH (CPC Scientific, HIST-035A) or a biotinylated H4K5ac/8ac/12ac/16ac (1-18) peptide (Epigentek, R-1008-200). For preliminary screens, 10 µL of a 4× protein stock (final assay concentration 0.07-7 µM for BRD4-BD1 and 0.1-10 µM for BRD4-BD2) was incubated with 10 µL of a 4× peptide stock (final assay concentration 100 nM) in technical triplicate. The plate was incubated at room temperature for 30 minutes. A bead solution containing 8 µg/mL of streptavidin-coated donor beads and 8 µg/mL of nickel-chelate acceptor beads (Revvity, AlphaScreen Histidine (Nickel Chelate) Detection Kit, 500 assay points, 6760619C) was prepared in the assay buffer. Under green-filtered lighting, 20 µL of the bead mixture was added to each well, and the plate was covered and incubated at room temperature for 1 hour. The luminescence of each well was quantified using the Alpha filter cube (Agilent, 1325000) on a BioTek Cytation 5 imaging reader (Agilent, 16277). The resulting Alpha counts were analyzed with GraphPad Prism. Alpha counts for initial screens were corrected by subtracting the Alpha counts from the average of the negative control samples (100 nM peptide alone and 10 µM protein alone). Corrected Alpha counts of BRD4-BD1/2 missense variants were then normalized to those of the wild-type bromodomains. For full titrations, 10 µL of a 4× protein stock (final assay concentration 0.001-7 µM for BRD4-BD1 and 0.001-1 µM for BRD4-BD2) was incubated with 10 µL of a 4× peptide stock (final assay concentration 100 nnM) in technical triplicate, and the assay was conducted as above. Raw Alpha counts were transferred to GraphPad Prism and fit to a sigmoidal non-linear regression, then normalized based on the bottom and top values of the fit, to determine the half-maximal effective concentration of binding (EC_{50}).

Public datasets used for ChIP-seq

Datasets for multiple transcription factors were obtained from public databases, including ENCODE, ChIP-Atlas, and NCBI GEO. This includes peaks for E2F6 (SRX190355, H1), HDAC2 (SRX100390, H1), MAX (SRX190354, H1), MYC (SRX150588, H1), RYBP (SRX3256865, H1), H3K14ac (SRX037086, NCCIT), H3K23ac (SRX17629284, H1) and H2A119Ub (SRX156117, H1). Same datasets were also used for bigwigs apart from CBX8 (ENCFF189EMD), EZH2 (ENCFF109KCQ), H3K23ac (this study) and H3K14ac (ENCFF079HBG), for which ENCODE bigwigs were used for plotting. For PCGF6, we used the GSE173690 dataset (PGP1 iPSC cell line), where the signal was merged across two replicates. A correlation heatmap of these TFs and histone marks, along with CUT&Tag or CUT&Run datasets, was generated using the multiBigwigSummary tool in deepTools [82], with genic promoters of protein-coding genes as the input BED file. Comparison of BRD4 CUT&Tag data at TSS of protein-coding genes and at active enhancers in H9 and H1 from SEDB 2.0 (super enhancer database) was done using deepTools. Other ENCODE datasets ENCFF285JOX (H3K27me3) and ENCFF548EWT (H3K4me3) bigwigs from H9-derived neurons were used for plotting and visualization.

RNA-seq

For Bulk RNA-seq, fastq files were subjected to QC and trimmed for adapters using Trim-galore, followed by mapping to hg38 reference using STAR-aligner[83] following Bluebee corall pipeline with these parameters: *--peOverlapNbasesMin 40 --peOverlapMMp 0.8 --outFilterType BySJout --outFilterMultimapNmax 200 --alignSJoverhangMin 8 --alignSJDBoverhangMin 1 --outFilterMismatchNmax 999 --outFilterMismatchNoverLmax 0.6 --alignIntronMin 20 --alignIntronMax 1000000 --limitOutSJcollapsed 5000000 --seedPerWindowNmax 10.* The counts obtained were then used for the differential expression analyses. For ZxH-treated cells, expression was compared at 4 h, 8 h, and 20 h. The count matrix was used for differential expression, followed by annotation of the DEGs using the integrated Differential Expression and Pathway analysis (iDEP2) tool with default filtration settings. After initial filtering for low coverage and data normalization, differential expression analysis was performed with DESeq2. The different comparisons used for RNA-seq analyses include ZxH (4hr, 8hr, or 12hr) vs DMSO in H9 cells; dTAGV-1 vs H9-WT (DMSO) (20hrs); and BRD4 BD2 mut1 vs WT in H9 cells or H9-derived Neurons. Functional annotation of up- or down-regulated genes was performed using shinyGO or Metascape. For all samples, except the ZxH 4-hour time-point (DMSO has two replicates), have a minimum of 3 replicates. For Gene Set Enrichment Analysis (GSEA), fold-change values were used in the Web-based Gene Set Analysis Toolkit (WEBGESTALT). Genes exhibiting significant deregulation (padj <0.05) in at least two ZxH treatment time points were filtered and used to compare log2fold change values as a heatmap using the Morpheus tool for ZxH time points, along with dTAGV-1 vs WT (Supplementary Data 2, Fig.1 Heatmap genes). The four clusters obtained were functionally annotated using ShinyGO for GO: Biological Processes, ARCHS4 TF-coexpression, and ARCHS4 Tissues. Similarly, common genes were identified as upregulated or downregulated in ZxH (8hrs) vs WT and in PCGF6-KO1 or KO2 vs WT. Genes upregulated/ downregulated in all three comparisons were annotated using Metascape (Supplementary Data 2, Metascape_res_genes_Fig.2c). MA-plots were generated for normalized expression against log2-fold-change, for all comparisons except bulk cerebral organoids, significant (p-adj < 0.05) bivalent genes were highlighted in red, other genes in blue, and all non-significant genes in grey. For a paired comparison of changes in expression of the bivalent genes across ZxH treatment time-points against WT, log2Fold change values were compared as an alluvial plot using gg-alluvial. Genes having a range between ± 0.5 were considered no-change, > 0.5 as upregulated and < -0.5 as down-regulated. We then performed GSEA for these common differentially expressed genes (Supplementary Data 2, GSEA for genes in Fig. 4b). Paired analysis of

genes showing similar directional changes in BRD4 mut1/WT and dTAGV-1/DMSO was compared using an upset plot and an XY scatterplot of fold-change values.

For bigwig generation, the individual mapped bam files were sorted and indexed using samtools, followed by bamCoverage (deepTools) with the option normaliseUsing RPKM and a bin size of 20 bp. Further, bigwigs for replicates across the same samples were merged, sorted and indexed with samtools, followed by bigwig generation as described above. To generate normalized bigwig files for BD2 Mut1 vs WT, bigwigCompare was used with a binsize of 20 and skipNAs, with log2 normalization. These signal files were used to plot or visualize on the genome browser.

scRNA-seq

Cellplex oligos (10x Genomics) were used for cell hashing, and scRNA-seq libraries were generated by using the NextGEM 3' v3.1 kit (10x Genomics). scRNA-seq libraries were sequenced with 150 bp paired-end reads at Novogene using the Novaseq X platform.

scATACseq

scATACseq libraries were generated using 10X Single Cell ATAC v2 reagents and sequenced with 50 bp paired-end reads, yielding 50 million reads per library at Novogene using the Illumina NextSeq platform.

scRNA-seq data analysis

scRNAseq data were mapped using CellRanger and reference GEX genome GRCh38 (2020-A) from 10x Genomics. The filtered matrix was filtered with DoubletFinder [84], assuming a 3.1% doublet formation rate and for nFeature_RNA>500 & percent.mt<10. After filtering, we had WT 3641 cells at d41 and 2541 at d63; mut2 3815 cells at d41 and 3899 at d63; and mut3 4293 at d41 and 4097 at d63. Data was then processed with Seurat 5.3.0 [85]. Data from UNOs at d41 and d63 were processed separately (in the same way as the merged data), then merged using *merge*, normalized using *NormalizeData and FindVariableFeatures*, and scaled with *ScaleData* using all genes and no regression [43]. To remove batch effects, we used CSS (cluster similarity spectrum) [41]. To do so, *cluster_sim_spectrum* was used with the argument *label_tag=" TimePoint"*. *RunUMAP* was then run on the CSS reduction, with the dims argument set to *1:ncol(Embeddings(obj," css*")), as described in the CSS vignette. Finally, the data were clustered first with *FindClusters* at a resolution of 0.2, and the clusters were manually annotated using markers from [43,44,86].

Mapping of scATACseq

scATACseq data were mapped using Cellranger-ATAC and the reference ARC genome GRCh38 (2020-A-2.0.0) from 10x Genomics. Data were then processed with ArchR [87] and following the ArchR manual (https://www.archrproject.com/bookdown/index.html). Briefly, arrows were created using minTSS=4 and minFrags=1000. Doublets were identified using *addDoubletScores* and *k =10*. After filtering, we had 4236 cells for WT and 4103 cells for BRD4 mut2. scRNAseq data were integrated into the scATACseq using *addGeneIntegrationMatrix*. Differentially accessible peaks were obtained with *addReproduciblePeak* using Macs2 and *getMarkerFeatures*, with log10(nfrags) as bias, between WT and BRD4mut2. Bigwig files were generated using *getGroupBW* with a tile size of 20 and normalized by the number of cells (nCells).

Motif enrichment analysis of scATAC-seq data

Normalized ATAC-seq bigwigs for BRD4-BD2 mutant/WT were generated using the deepTools compareBigwig function for each cluster. We filtered for differentially accessible (DA) open peaks in

mutants within each cluster, applying a threshold of p-value < 0.01 and log2FoldChange> 0.5. For motif enrichment analysis, we used the gimme maelstrom tool to identify differentially enriched motifs within each cluster for the open peaks. We performed central motif enrichment analysis using the Centrimo tool (MEME suite) on the DA open peaks in the BRD4 BD2 mutant for each cell cluster. Data plotted for Gimme maelstrom and Centrimo are listed in Supplementary Data 3.

scCUT&Tag data

scCUT&Tag data from Zenk et al were used to determine which genes were bivalently marked in UNO populations [44]. We decided to use the merge dataset from d35, d60, and d120, and the BigWig files for H3K4me3, H3K27ac, and H3K27me3 at those time points, which were generated using *getGroupBw* from archR with a tile size of 100 and normalized by reads in TSS (ReadsInTSS).

Acknowledgements

We thank Wendy Bickmore and Rob Illingworth (University of Edinburgh), Elena Torlai Triglia, Mirjana Efremova and other QMUL epigenetics centre members for their discussion and feedback. We thank Sara Badodi, Radu Zabet, Hemanth Tummala (QMUL), Michael-Christopher Keogh (EpiCypher), and Silvia Santos (Francis Crick Institute) for sharing reagents. We thank the Blizard core facilities, including the Genome Centre, for scRNA-seq and scATAC-seq library preparation. This research utilized Queen Mary's Apocrita HPC facility, supported by QMUL Research-IT.

Funding: Medical Research Council UKRI/MRC grants (MR/T000783/1 and MR/X008479/1) and Barts charity grant (G-002379).

Author contributions

Conceptualization, PMM, MP, and FB; Methodology, FB, MP, PMM, ZS, NA, and AM; Software, MP and FB; Investigation, FB, MP, PMM, ZSZ, NA, AI, PD, DP, MDL, and KLB; Writing – Original Draft, PMM, FB, and MP; Visualisation, FB, MP, MDL, and PMM; Supervision, PMM, DN, and BCS; Funding Acquisition, PMM.

Data availability: Data is submitted to NCBI GEO and the Broad single-cell portals. Available with the following accession numbers: CUT&Tag and CUT&Run data; GSE313479.
Bulk RNAseq; GSE313810,
scRNAseq:URL: https://singlecell.broadinstitute.org/single_cell/reviewer_access/54079f88-4f30-4036-b567-0d71264bb526
scATACseq; GSE314451

Declaration: The authors declare no conflict of interest.

References

1. **Sanchez, R., Meslamani, J., and Zhou, M.M. (2014). The bromodomain: From epigenome reader to druggable target. Biochimica et Biophysica Acta - Gene Regulatory Mechanisms. https://doi.org/10.1016/j.bbagrm.2014.03.011**
2. **Hsu, S.C., Gilgenast, T.G., Bartman, C.R., Edwards, C.R., Stonestrom, A.J., Huang, P., Emerson, D.J., Evans, P., Werner, M.T., Keller, C.A., et al. (2017). The BET Protein BRD2 Cooperates with CTCF to Enforce Transcriptional and Architectural Boundaries. Mol. Cell *66*, 102-116.e7. https://doi.org/10.1016/j.molcel.2017.02.027.**
3. **Daneshvar, K., Ardehali, M.B., Klein, I.A., Hsieh, F.K., Kratkiewicz, A.J., Mahpour, A., Cancelliere, S.O.L., Zhou, C., Cook, B.M., Li, W., et al. (2020). lncRNA DIGIT and BRD3 protein form phase-separated condensates to regulate endoderm differentiation. Nat. Cell Biol. *22*, 1211–1222. https://doi.org/10.1038/s41556-020-0572-2.**

4. Linares-Saldana, R., Kim, W., Bolar, N.A., Zhang, H., Koch-Bojalad, B.A., Yoon, S., Shah, P.P., Karnay, A., Park, D.S., Luppino, J.M., et al. (2021). BRD4 orchestrates genome folding to promote neural crest differentiation. Nat. Genet. *53*, 1480–1492. https://doi.org/10.1038/s41588-021-00934-8.
5. Donati, B., Lorenzini, E., and Ciarrocchi, A. (2018). BRD4 and Cancer: Going beyond transcriptional regulation. Preprint at BioMed Central Ltd., https://doi.org/10.1186/s12943-018-0915-9 https://doi.org/10.1186/s12943-018-0915-9.
6. Shi, J., and Vakoc, C.R. (2014). The Mechanisms behind the Therapeutic Activity of BET Bromodomain Inhibition. Preprint at Cell Press, https://doi.org/10.1016/j.molcel.2014.05.016 https://doi.org/10.1016/j.molcel.2014.05.016.
7. Lovén, J., Hoke, H.A., Lin, C.Y., Lau, A., Orlando, D.A., Vakoc, C.R., Bradner, J.E., Lee, T.I., and Young, R.A. (2013). Selective inhibition of tumor oncogenes by disruption of super-enhancers. Cell *153*, 320–334. https://doi.org/10.1016/j.cell.2013.03.036.
8. Sabari, B.R., Dall'Agnese, A., Boija, A., Klein, I.A., Coffey, E.L., Shrinivas, K., Abraham, B.J., Hannett, N.M., Zamudio, A. V., Manteiga, J.C., et al. (2018). Coactivator condensation at super-enhancers links phase separation and gene control. Science (1979). *361*. https://doi.org/10.1126/science.aar3958.
9. Han, X., Yu, D., Gu, R., Jia, Y., Wang, Q., Jaganathan, A., Yang, X., Yu, M., Babault, N., Zhao, C., et al. (2020). Roles of the BRD4 short isoform in phase separation and active gene transcription. Nat. Struct. Mol. Biol. *27*, 333–341. https://doi.org/10.1038/s41594-020-0394-8.
10. Conrad, R.J., Fozouni, P., Thomas, S., Sy, H., Zhang, Q., Zhou, M.M., and Ott, M. (2017). The Short Isoform of BRD4 Promotes HIV-1 Latency by Engaging Repressive SWI/SNF Chromatin-Remodeling Complexes. Mol. Cell *67*, 1001-1012.e6. https://doi.org/10.1016/j.molcel.2017.07.025.
11. Wu, S.Y., Lee, A.Y., Hou, S.Y., Kemper, J.K., Erdjument-Bromage, H., Tempst, P., and Chiang, C.M. (2006). Brd4 links chromatin targeting to HPV transcriptional silencing. Genes Dev. *20*, 2383–2396. https://doi.org/10.1101/gad.1448206.
12. Zhao, L., Wang, Y., Jaganathan, A., Sun, Y., Ma, N., Li, N., Han, X., Sun, X., Yi, H., Fu, S., et al. (2023). BRD4□PRC2 represses transcription of T□helper 2□specific negative regulators during T□cell differentiation. EMBO J. *42*. https://doi.org/10.15252/embj.2022111473.
13. Sakamaki, J. ichi, Wilkinson, S., Hahn, M., Tasdemir, N., O'Prey, J., Clark, W., Hedley, A., Nixon, C., Long, J.S., New, M., et al. (2017). Bromodomain Protein BRD4 Is a Transcriptional Repressor of Autophagy and Lysosomal Function. Mol. Cell *66*, 517-532.e9. https://doi.org/10.1016/j.molcel.2017.04.027.
14. Kang, H., Jung, Y.L., McElroy, K.A., Zee, B.M., Wallace, H.A., Woolnough, J.L., Park, P.J., and Kuroda, M.I. (2017). Bivalent complexes of PRC1 with orthologs of BRD4 and MOZ/MORF target developmental genes in Drosophila. Genes Dev. *31*, 1988–2002. https://doi.org/10.1101/gad.305987.117.
15. Fallah, M.S., Szarics, D., Robson, C.M., and Eubanks, J.H. (2021). Impaired Regulation of Histone Methylation and Acetylation Underlies Specific Neurodevelopmental Disorders. Preprint at Frontiers Media S.A., https://doi.org/10.3389/fgene.2020.613098 https://doi.org/10.3389/fgene.2020.613098.
16. Olley, G., Ansari, M., Bengani, H., Grimes, G.R., Rhodes, J., Von Kriegsheim, A., Blatnik, A., Stewart, F.J., Wakeling, E., Carroll, N., et al. (2018). BRD4 interacts with NIPBL and BRD4 is mutated in a Cornelia de Lange-like syndrome. Nat. Genet. *50*, 329–332. https://doi.org/10.1038/s41588-018-0042-y.
17. Deardorff, M.A., Bando, M., Nakato, R., Watrin, E., Itoh, T., Minamino, M., Saitoh, K., Komata, M., Katou, Y., Clark, D., et al. (2012). HDAC8 mutations in Cornelia de Lange syndrome affect the cohesin acetylation cycle. Nature *489*, 313–317. https://doi.org/10.1038/nature11316.
18. Basilicata, M.F., Bruel, A.L., Semplicio, G., Valsecchi, C.I.K., Aktaş, T., Duffourd, Y., Rumpf, T., Morton, J., Bache, I., Szymanski, W.G., et al. (2018). De novo mutations in

MSL3 cause an X-linked syndrome marked by impaired histone H4 lysine 16 acetylation. Nat. Genet. *50*, 1442–1451. https://doi.org/10.1038/s41588-018-0220-y.

19. **Korb, E., Herre, M., Zucker-Scharff, I., Darnell, R.B., and Allis, C.D. (2015). BET protein Brd4 activates transcription in neurons and BET inhibitor Jq1 blocks memory in mice. Nat. Neurosci. *18*, 1464–1473. https://doi.org/10.1038/nn.4095.**
20. **Olley, G., Pradeepa, M.M., Grimes, G.R., Piquet, S., Polo, S.E., FitzPatrick, D.R., Bickmore, W.A., and Boumendil, C. (2021). Cornelia de Lange syndrome-associated mutations cause a DNA damage signalling and repair defect. Nat. Commun. *12*. https://doi.org/10.1038/s41467-021-23500-6.**
21. **Nowak, R.P., Deangelo, S.L., Buckley, D., He, Z., Donovan, K.A., An, J., Safaee, N., Jedrychowski, M.P., Ponthier, C.M., Ishoey, M., et al. (2018). Plasticity in binding confers selectivity in ligand-induced protein degradation article. Nat. Chem. Biol. *14*, 706–714. https://doi.org/10.1038/s41589-018-0055-y.**
22. **Nabet, B., Roberts, J.M., Buckley, D.L., Paulk, J., Dastjerdi, S., Yang, A., Leggett, A.L., Erb, M.A., Lawlor, M.A., Souza, A., et al. (2018). The dTAG system for immediate and target-specific protein degradation. Nat. Chem. Biol. *14*, 431–441. https://doi.org/10.1038/s41589-018-0021-8.**
23. **Azuara, V., Perry, P., Sauer, S., Spivakov, M., Jørgensen, H.F., John, R.M., Gouti, M., Casanova, M., Warnes, G., Merkenschlager, M., et al. (2006). Chromatin signatures of pluripotent cell lines. Nature cell Biology DOI: 10/1038 ncb1403**
24. **Bernstein, B.E., Mikkelsen, T.S., Xie, X., Kamal, M., Huebert, D.J., Cuff, J., Fry, B., Meissner, A., Wernig, M., Plath, K., et al. (2006). A Bivalent Chromatin Structure Marks Key Developmental Genes in Embryonic Stem Cells. Cell *125*, 315–326. https://doi.org/10.1016/j.cell.2006.02.041.**
25. **Lan, X., Ding, S., Zhang, T., Yi, Y., Li, C., Jin, W., Chen, J., Liang, K., Wang, H., and Jiang, W. (2022). PCGF6 controls neuroectoderm specification of human pluripotent stem cells by activating SOX2 expression. Nat. Commun. *13*. https://doi.org/10.1038/s41467-022-32295-z.**
26. **Stielow, B., Finkernagel, F., Stiewe, T., Nist, A., and Suske, G. (2018). MGA, L3MBTL2 and E2F6 determine genomic binding of the non-canonical Polycomb repressive complex PRC1.6. PLoS Genet. *14*. https://doi.org/10.1371/journal.pgen.1007193.**
27. **Zijlmans, D.W., Stelloo, S., Bax, D., Yordanov, Y., Toebosch, P., Raas, M.W.D., Verhelst, S., Lamers, L.A., Baltissen, M.P.A., Jansen, P.W.T.C., et al. (2025). PRC1 and PRC2 proximal interactome in mouse embryonic stem cells. Cell Rep. *44*. https://doi.org/10.1016/j.celrep.2025.115362.**
28. **Arnold, M., Bressin, A., Jasnovidova, O., Meierhofer, D., and Mayer, A. (2021). A BRD4-mediated elongation control point primes transcribing RNA polymerase II for 3′-processing and termination. Mol. Cell *81*, 3589-3603.e13. https://doi.org/10.1016/j.molcel.2021.06.026.**
29. **Bressin, A., Jasnovidova, O., Arnold, M., Altendorfer, E., Trajkovski, F., Kratz, T.A., Handzlik, J.E., Hnisz, D., and Mayer, A. (2023). High-sensitive nascent transcript sequencing reveals BRD4-specific control of widespread enhancer and target gene transcription. Nat. Commun. *14*. https://doi.org/10.1038/s41467-023-40633-y.**
30. **Bryan, E., Valsakumar, D., Idigo, N.J., Warburton, M., Webb, K.M., McLaughlin, K.A., Spanos, C., Lenci, S., Major, V., Ambrosi, C., et al. (2024). Nucleosomal asymmetry shapes histone mark binding and promotes poising at bivalent domains. Mol. Cell. https://doi.org/10.1016/j.molcel.2024.12.002.**
31. **Filippakopoulos, P., Picaud, S., Mangos, M., Keates, T., Lambert, J.P., Barsyte-Lovejoy, D., Felletar, I., Volkmer, R., Müller, S., Pawson, T., et al. (2012). Histone recognition and large-scale structural analysis of the human bromodomain family. Cell *149*, 214–231. https://doi.org/10.1016/j.cell.2012.02.013.**
32. **Delmore, J.E., Issa, G.C., Lemieux, M.E., Rahl, P.B., Shi, J., Jacobs, H.M., Kastritis, E., Gilpatrick, T., Paranal, R.M., Qi, J., et al. (2011). BET bromodomain inhibition as a therapeutic strategy to target c-Myc. Cell *146*, 904–917. https://doi.org/10.1016/j.cell.2011.08.017.**

33. Pal, D., Patel, M., Boulet, F., Sundarraj, J., Grant, O.A., Branco, M.R., Basu, S., Santos, S.D.M., Zabet, N.R., Scaffidi, P., et al. (2023). H4K16ac activates the transcription of transposable elements and contributes to their cis-regulatory function. Nat. Struct. Mol. Biol. https://doi.org/10.1038/s41594-023-01016-5.
34. Pradeepa, M.M., Grimes, G.R., Kumar, Y., Olley, G., Taylor, G.C.A., Schneider, R., and Bickmore, W.A. (2016). Histone H3 globular domain acetylation identifies a new class of enhancers. Nat. Genet. *48*, 681–686. https://doi.org/10.1038/ng.3550.
35. Taylor, G.C.A., Eskeland, R., Hekimoglu-Balkan, B., Pradeepa, M.M., and Bickmore, W.A. (2013). H4K16 acetylation marks active genes and enhancers of embryonic stem cells, but does not alter chromatin compaction. Genome Res. *23*, 2053–2065. https://doi.org/10.1101/gr.155028.113.
36. Lancaster, M.A., and Knoblich, J.A. (2014). Generation of cerebral organoids from human pluripotent stem cells. Nat. Protoc. *9*, 2329–2340. https://doi.org/10.1038/nprot.2014.158.
37. Lancaster, M.A., Renner, M., Martin, C.A., Wenzel, D., Bicknell, L.S., Hurles, M.E., Homfray, T., Penninger, J.M., Jackson, A.P., and Knoblich, J.A. (2013). Cerebral organoids model human brain development and microcephaly. Nature *501*, 373–379. https://doi.org/10.1038/nature12517.
38. Lindenhofer, D., Haendeler, S., Esk, C., Littleboy, J.B., Brunet Avalos, C., Naas, J., Pflug, F.G., van de Ven, E.G.P., Reumann, D., Baffet, A.D., et al. (2024). Cerebral organoids display dynamic clonal growth and tunable tissue replenishment. Nat. Cell Biol. *26*, 710–718. https://doi.org/10.1038/s41556-024-01412-z.
39. Bahrami, S., and Drabløs, F. (2016). Gene regulation in the immediate-early response process. Preprint at Elsevier Ltd, https://doi.org/10.1016/j.jbior.2016.05.001
40. Lanahan, A., and Worley, P. (1998). Immediate-Early Genes and Synaptic Function.
41. He, Z., Brazovskaja, A., Ebert, S., Camp, J.G., and Treutlein, B. (2020). CSS: cluster similarity spectrum integration of single-cell genomics data. Genome Biol. *21*. https://doi.org/10.1186/s13059-020-02147-4.
42. Becht, E., McInnes, L., Healy, J., Dutertre, C.A., Kwok, I.W.H., Ng, L.G., Ginhoux, F., and Newell, E.W. (2019). Dimensionality reduction for visualizing single-cell data using UMAP. Nat. Biotechnol. *37*, 38–47. https://doi.org/10.1038/nbt.4314.
43. Kanton, S., Treutlein, B., and Camp, J.G. (2020). Single-cell genomic analysis of human cerebral organoids. In Methods in Cell Biology (Academic Press Inc.), pp. 229–256. https://doi.org/10.1016/bs.mcb.2020.03.013.
44. Zenk, F., Fleck, J.S., Jansen, S.M.J., Kashanian, B., Eisinger, B., Santel, M., Dupré, J.S., Camp, J.G., and Treutlein, B. (2024). Single-cell epigenomic reconstruction of developmental trajectories from pluripotency in human neural organoid systems. Nat. Neurosci. *27*, 1376–1386. https://doi.org/10.1038/s41593-024-01652-0.
45. Yap, E.L., and Greenberg, M.E. (2018). Activity-Regulated Transcription: Bridging the Gap between Neural Activity and Behavior. Neuron https://doi.org/10.1016/j.neuron.2018.10.013
46. Philippidou, P., and Dasen, J.S. (2013). Hox Genes: Choreographers in Neural Development, Architects of Circuit Organization. Neuron https://doi.org/10.1016/j.neuron.2013.09.020
47. Hurlin, P.J., Eirı`kur, E., Steingrı`msson, S., Copeland, N.G., Jenkins, N.A., and Eisenman, R.N. (1999). Mga, a dual-specificity transcription factor that interacts with Max and contains a T-domain DNA-binding motif. EMBO J. 1999 Dec 15;18(24):7019-28. doi: 10.1093/emboj/18.24.7019.
48. Fursova, N.A., Blackledge, N.P., Nakayama, M., Ito, S., Koseki, Y., Farcas, A.M., King, H.W., Koseki, H., and Klose, R.J. (2019). Synergy between Variant PRC1 Complexes Defines Polycomb-Mediated Gene Repression. Mol. Cell *74*, 1020-1036.e8. https://doi.org/10.1016/j.molcel.2019.03.024.
49. Scelfo, A., Fernández-Pérez, D., Tamburri, S., Zanotti, M., Lavarone, E., Soldi, M., Bonaldi, T., Ferrari, K.J., and Pasini, D. (2019). Functional Landscape of PCGF Proteins

Reveals Both RING1A/B-Dependent-and RING1A/B-Independent-Specific Activities. Mol. Cell *74*, 1037-1052.e7. https://doi.org/10.1016/j.molcel.2019.04.002.

50. McGivern, B., Morrow, M.M., Torti, E., McWalter, K., Wentzensen, I.M., Monaghan, K.G., Gerard, A., Robak, L., Chitayat, D., Botsford, C., et al. (2025). MGA-related syndrome: A proposed novel disorder. Human Genetics and Genomics Advances *6*. https://doi.org/10.1016/j.xhgg.2024.100387.

51. Karmodiya, K., Krebs, A.R., Oulad-Abdelghani, M., Kimura, H., and Tora, L. (2012). H3K9 and H3K14 acetylation co-occur at many gene regulatory elements, while H3K14ac marks a subset of inactive inducible promoters in mouse embryonic stem cells. BMC Genomics *13*. https://doi.org/10.1186/1471-2164-13-424.

52. Lukauskas, S., Tvardovskiy, A., Nguyen, N. V., Stadler, M., Faull, P., Ravnsborg, T., Özdemir Aygenli, B., Dornauer, S., Flynn, H., Lindeboom, R.G.H., et al. (2024). Decoding chromatin states by proteomic profiling of nucleosome readers. Nature *627*, 671–679. https://doi.org/10.1038/s41586-024-07141-5.

53. Jouret, G., Heide, S., Sorlin, A., Faivre, L., Chantot-Bastaraud, S., Beneteau, C., Denis-Musquer, M., Turnpenny, P.D., Coutton, C., Vieville, G., et al. (2022). Understanding the new BRD4-related syndrome: Clinical and genomic delineation with an international cohort study. Clin. Genet. *102*, 117–122. https://doi.org/10.1111/cge.14141.

54. Li, J., Ma, J., Meng, G., Lin, H., Wu, S., Wang, J., Luo, J., Xu, X., Tough, D., Lindon, M., et al. (2016). BET bromodomain inhibition promotes neurogenesis while inhibiting gliogenesis in neural progenitor cells. Stem Cell Res. *17*, 212–221. https://doi.org/10.1016/j.scr.2016.07.006.

55. Huber, P.B., Rao, A., and LaBonne, C. (2024). BET activity plays an essential role in control of stem cell attributes in Xenopus. Development (Cambridge) *151*. https://doi.org/10.1242/dev.202990.

56. Groza, T., Gomez Lopez, F.L., Mashhadi, H.H., Muñoz-Fuentes, V., Gunes, O., Wilson, R., Cacheiro, P., Frost, A., Keskivali-Bond, P., Vardal, B., et al. (2023). The International Mouse Phenotyping Consortium: comprehensive knockout phenotyping underpinning the study of human disease. Nucleic Acids Res. *51*, D1038–D1045. https://doi.org/10.1093/nar/gkac972.

57. Jin, H.S., Kim, J., Kwak, W., Jeong, H., Lim, G. Bin, and Lee, C.G. (2017). Identification of a novel mutation in brd4 that causes autosomal dominant syndromic congenital cataracts associated with other neuro-skeletal anomalies. PLoS One *12*. https://doi.org/10.1371/journal.pone.0169226.

58. Doyle, L.A., Unlu Bektas, F., Chatzantonaki, E., Repton, C., Derrien, A., and Illingworth, R.S. (2022). RINGs, DUBs and Abnormal Brain Growth—Histone H2A Ubiquitination in Brain Development and Disease. Preprint at MDPI, https://doi.org/10.3390/epigenomes6040042 https://doi.org/10.3390/epigenomes6040042.

59. Gibson, W.T., Hood, R.L., Zhan, S.H., Bulman, D.E., Fejes, A.P., Moore, R., Mungall, A.J., Eydoux, P., Babul-Hirji, R., An, J., et al. (2012). Mutations in EZH2 cause weaver syndrome. Am. J. Hum. Genet. *90*, 110–118. https://doi.org/10.1016/j.ajhg.2011.11.018.

60. Cohen, A.S.A., Tuysuz, B., Shen, Y., Bhalla, S.K., Jones, S.J.M., and Gibson, W.T. (2015). A novel mutation in EED associated with overgrowth. J. Hum. Genet. *60*, 339–342. https://doi.org/10.1038/jhg.2015.26.

61. Lederer, D., Grisart, B., Digilio, M.C., Benoit, V., Crespin, M., Ghariani, S.C., Maystadt, I., Dallapiccola, B., and Verellen-Dumoulin, C. (2012). Deletion of KDM6A, a histone demethylase interacting with MLL2, in three patients with kabuki syndrome. Am. J. Hum. Genet. *90*, 119–124. https://doi.org/10.1016/j.ajhg.2011.11.021.

62. Pereira, J.D., Sansom, S.N., Smith, J., Dobenecker, M.W., Tarakhovsky, A., and Livesey, F.J. (2010). Ezh2, the histone methyltransferase of PRC2, regulates the balance between self-renewal and differentiation in the cerebral cortex. Proc. Natl. Acad. Sci. U. S. A. *107*, 15957–15962. https://doi.org/10.1073/pnas.1002530107.

63. Telley, L., Agirman, G., Prados, J., Amberg, N., Fièvre, S., Oberst, P., Bartolini, G., Vitali, I., Cadilhac, C., Hippenmeyer, S., et al. (2019). Temporal patterning of apical

progenitors and their daughter neurons in the developing neocortex. Science (1979). *364*. https://doi.org/10.1126/science.aav2522.

64. Mätlik, K., Govek, E.E., and Hatten, M.E. (2025). Histone bivalency in CNS development. Preprint at Cold Spring Harbor Laboratory Press, https://doi.org/10.1101/gad.352306.124 https://doi.org/10.1101/gad.352306.124.

65. Mätlik, K., Govek, E.E., Paul, M.R., Allis, C.D., and Hatten, M.E. (2023). Histone bivalency regulates the timing of cerebellar granule cell development. Genes Dev. *37*, 570–589. https://doi.org/10.1101/gad.350594.123.

66. Quinonez, S.C., and Innis, J.W. (2014). Human HOX gene disorders. Preprint at Academic Press Inc., https://doi.org/10.1016/j.ymgme.2013.10.012 https://doi.org/10.1016/j.ymgme.2013.10.012.

67. Blank, M.C., Grinberg, I., Aryee, E., Laliberte, C., Chizhikov, V. V., Mark Henkelman, R., and Millen, K.J. (2011). Multiple developmental programs are altered by loss of Zic1 and Zic4 to cause Dandy-Walker malformation cerebellar pathogenesis. Development *138*, 1207–1216. https://doi.org/10.1242/dev.054114.

68. Angelozzi, M., and Lefebvre, V. (2019). SOXopathies: Growing Family of Developmental Disorders Due to SOX Mutations. Preprint at Elsevier Ltd, https://doi.org/10.1016/j.tig.2019.06.003 https://doi.org/10.1016/j.tig.2019.06.003.

69. Kikkawa, T., Casingal, C.R., Chun, S.H., Shinohara, H., Hiraoka, K., and Osumi, N. (2019). The role of Pax6 in brain development and its impact on pathogenesis of autism spectrum disorder. Brain Research https://doi.org/10.1016/j.brainres.2018.02.041

70. Shoichet, S.A., Kunde, S.A., Viertel, P., Schell-Apacik, C., von Voss, H., Tommerup, N., Ropers, H.H., and Kalscheuer, V.M. (2005). Haploinsufficiency of novel FOXG1B variants in a patient with severe mental retardation, brain malformations and microcephaly. Hum. Genet. *117*, 536–544. https://doi.org/10.1007/s00439-005-1310-3.

71. Gong, F., Chiu, L.Y., Cox, B., Aymard, F., Clouaire, T., Leung, J.W., Cammarata, M., Perez, M., Agarwal, P., Brodbelt, J.S., et al. (2015). Screen identifies bromodomain protein ZMYND8 in chromatin recognition of transcription-associated DNA damage that promotes homologous recombination. Genes Dev. *29*, 197–211. https://doi.org/10.1101/gad.252189.114.

72. Bracken, AP., Dietrich, N., Pasini D., Hansen, KH., and Helin K., Genome-wide mapping of Polycomb target genes unravels their roles in cell fate transitions GENES & DEVELOPMENT 20:1123–1136

73. Clijsters, L., Hoencamp, C., Calis, J.J.A., Marzio, A., Handgraaf, S.M., Cuitino, M.C., Rosenberg, B.R., Leone, G., and Pagano, M. (2019). Cyclin F Controls Cell-Cycle Transcriptional Outputs by Directing the Degradation of the Three Activator E2Fs. Mol. Cell *74*, 1264-1277.e7. https://doi.org/10.1016/j.molcel.2019.04.010.

74. Trojer, P., Li, G., Sims, R.J., Vaquero, A., Kalakonda, N., Boccuni, P., Lee, D., Erdjument-Bromage, H., Tempst, P., Nimer, S.D., et al. (2007). L3MBTL1, a Histone-Methylation-Dependent Chromatin Lock. Cell *129*, 915–928. https://doi.org/10.1016/j.cell.2007.03.048.

75. Meers, M.P., Bryson, T.D., Henikoff, J.G., and Henikoff, S. (2019). Improved cut&run chromatin profiling tools. Elife *8*. https://doi.org/10.7554/eLife.46314.001.

76. Kaya-Okur, H.S., Wu, S.J., Codomo, C.A., Pledger, E.S., Bryson, T.D., Henikoff, J.G., Ahmad, K., and Henikoff, S. (2019). CUT&Tag for efficient epigenomic profiling of small samples and single cells. Nat. Commun. *10*. https://doi.org/10.1038/s41467-019-09982-5.

77. Langmead, B., and Salzberg, S.L. (2012). Fast gapped-read alignment with Bowtie 2. Nat. Methods *9*, 357–359. https://doi.org/10.1038/nmeth.1923.

78. Danecek, P., Bonfield, J.K., Liddle, J., Marshall, J., Ohan, V., Pollard, M.O., Whitwham, A., Keane, T., McCarthy, S.A., and Davies, R.M. (2021). Twelve years of SAMtools and BCFtools. Gigascience *10*. https://doi.org/10.1093/gigascience/giab008.

79. Meers, M.P., Tenenbaum, D., and Henikoff, S. (2019). Peak calling by Sparse Enrichment Analysis for CUT&RUN chromatin profiling. Epigenetics Chromatin *12*. https://doi.org/10.1186/s13072-019-0287-4.

80. Zheng, R., Wan, C., Mei, S., Qin, Q., Wu, Q., Sun, H., Chen, C.H., Brown, M., Zhang, X., Meyer, C.A., et al. (2019). Cistrome Data Browser: Expanded datasets and new tools for gene regulatory analysis. Nucleic Acids Res. *47*, D729–D735. https://doi.org/10.1093/nar/gky1094.

81. Court, F., and Arnaud, P. (2017). Oncotarget 4110 www.impactjournals.com/oncotarget An annotated list of bivalent chromatin regions in human ES cells: a new tool for cancer epigenetic research.

82. Ramírez, F., Dündar, F., Diehl, S., Grüning, B.A., and Manke, T. (2014). DeepTools: A flexible platform for exploring deep-sequencing data. Nucleic Acids Res. *42*. https://doi.org/10.1093/nar/gku365.

83. Dobin, A., Davis, C.A., Schlesinger, F., Drenkow, J., Zaleski, C., Jha, S., Batut, P., Chaisson, M., and Gingeras, T.R. (2013). STAR: Ultrafast universal RNA-seq aligner. Bioinformatics *29*, 15–21. https://doi.org/10.1093/bioinformatics/bts635.

84. Zheng, G.X.Y., Terry, J.M., Belgrader, P., Ryvkin, P., Bent, Z.W., Wilson, R., Ziraldo, S.B., Wheeler, T.D., McDermott, G.P., Zhu, J., et al. (2017). Massively parallel digital transcriptional profiling of single cells. Nat. Commun. *8*. https://doi.org/10.1038/ncomms14049.

85. Hao, Y., Stuart, T., Kowalski, M.H., Choudhary, S., Hoffman, P., Hartman, A., Srivastava, A., Molla, G., Madad, S., Fernandez-Granda, C., et al. (2024). Dictionary learning for integrative, multimodal and scalable single-cell analysis. Nat. Biotechnol. *42*, 293–304. https://doi.org/10.1038/s41587-023-01767-y.

86. La Manno, G., Soldatov, R., Zeisel, A., Braun, E., Hochgerner, H., Petukhov, V., Lidschreiber, K., Kastriti, M.E., Lönnerberg, P., Furlan, A., et al. (2018). RNA velocity of single cells. Nature *560*, 494–498. https://doi.org/10.1038/s41586-018-0414-6.

87. Granja, J.M., Corces, M.R., Pierce, S.E., Bagdatli, S.T., Choudhry, H., Chang, H.Y., and Greenleaf, W.J. (2021). ArchR is a scalable software package for integrative single-cell chromatin accessibility analysis. Nat. Genet. *53*, 403–411. https://doi.org/10.1038/s41588-021-00790-6.